Measurement of the production cross-section of positive pions in the collision of 8.9 GeV/c protons on beryllium

HARP Collaboration

February 15, 2007

Abstract

The double-differential production cross-section of positive pions, $d^2\sigma^{\pi^+}/dpd\Omega$, measured in the HARP experiment is presented. The incident particles are 8.9 GeV/c protons directed onto a beryllium target with a nominal thickness of 5% of a nuclear interaction length. The measured cross-section has a direct impact on the prediction of neutrino fluxes for the MiniBooNE and SciBooNE experiments at Fermilab. After cuts, 13 million protons on target produced about 96,000 reconstructable secondary tracks which were used in this analysis. Cross-section results are presented in the kinematic range 0.75 GeV/$c \le p_\pi \le 6.5$ GeV/c and 30 mrad $\le \theta_\pi \le 210$ mrad in the laboratory frame.

HARP collaboration

M.G. Catanesi, E. Radicioni

Università degli Studi e Sezione INFN, Bari, Italy

R. Edgecock, M. Ellis[1], S. Robbins[2,3], F.J.P. Soler[4]

Rutherford Appleton Laboratory, Chilton, Didcot, UK

C. Gößling

Institut für Physik, Universität Dortmund, Germany

S. Bunyatov, G. Chelkov, D. Dedovitch, M. Gostkin, A. Guskov, D. Khartchenko, A. Krasnoperov, Z. Kroumchtein, Y. Nefedov, B. Popov[5], V. Serdiouk, V. Tereshchenko, A. Zhemchugov

Joint Institute for Nuclear Research, JINR Dubna, Russia

E. Di Capua, G. Vidal–Sitjes[6,7]

Università degli Studi e Sezione INFN, Ferrara, Italy

A. Artamonov[8], P. Arce[9], S. Giani, S. Gilardoni[6], P. Gorbunov[8,10], A. Grant, A. Grossheim[6,11], P. Gruber[6,12], V. Ivanchenko[13], A. Kayis-Topaksu[14], J. Panman, I. Papadopoulos, J. Pasternak[6], E. Tcherniaev, I. Tsukerman[8], R. Veenhof, C. Wiebusch[15], P. Zucchelli[10,16]

CERN, Geneva, Switzerland

A. Blondel, S. Borghi[17], M. Campanelli, M.C. Morone[18], G. Prior[6,19], R. Schroeter

Section de Physique, Université de Genève, Switzerland

R. Engel, C. Meurer

Institut für Physik, Universität Karlsruhe, Germany

I. Kato[11,20]

University of Kyoto, Japan

U. Gastaldi

Laboratori Nazionali di Legnaro dell' INFN, Legnaro, Italy

G. B. Mills[21]

Los Alamos National Laboratory, Los Alamos, USA

J.S. Graulich[22], G. Grégoire

Institut de Physique Nucléaire, UCL, Louvain-la-Neuve, Belgium

M. Bonesini, A. De Min, F. Ferri, M. Paganoni, F. Paleari

Università degli Studi e Sezione INFN, Milano, Italy

M. Kirsanov

Institute for Nuclear Research, Moscow, Russia

A. Bagulya, V. Grichine, N. Polukhina

P. N. Lebedev Institute of Physics (FIAN), Russian Academy of Sciences, Moscow, Russia

V. Palladino

Università "Federico II" e Sezione INFN, Napoli, Italy

L. Coney[21], D. Schmitz[21]

Columbia University, New York, USA

G. Barr, A. De Santo[23], C. Pattison, K. Zuber[24]

Nuclear and Astrophysics Laboratory, University of Oxford, UK

F. Bobisut, D. Gibin, A. Guglielmi, M. Mezzetto

Università degli Studi e Sezione INFN, Padova, Italy

J. Dumarchez, F. Vannucci

LPNHE, Universités de Paris VI et VII, Paris, France

V. Ammosov, V. Koreshev, A. Semak, V. Zaets

Institute for High Energy Physics, Protvino, Russia

U. Dore

Università "La Sapienza" e Sezione INFN Roma I, Roma, Italy

D. Orestano, F. Pastore, A. Tonazzo, L. Tortora

Università degli Studi e Sezione INFN Roma III, Roma, Italy

C. Booth, C. Buttar[4], P. Hodgson, L. Howlett

Dept. of Physics, University of Sheffield, UK

M. Bogomilov, M. Chizhov, D. Kolev, R. Tsenov

Faculty of Physics, St. Kliment Ohridski University, Sofia, Bulgaria

S. Piperov, P. Temnikov

Institute for Nuclear Research and Nuclear Energy, Academy of Sciences, Sofia, Bulgaria

M. Apollonio, P. Chimenti, G. Giannini, G. Santin[25]

Università degli Studi e Sezione INFN, Trieste, Italy

J. Burguet–Castell, A. Cervera–Villanueva, J.J. Gómez–Cadenas, J. Martín–Albo, P. Novella, M. Sorel, A. Tornero

Instituto de Física Corpuscular, IFIC, CSIC and Universidad de Valencia, Spain

[1]Now at FNAL, Batavia, Illinois, USA.

[2]Jointly appointed by Nuclear and Astrophysics Laboratory, University of Oxford, UK.

[3]Now at Codian Ltd., Langley, Slough, UK.

[4]Now at University of Glasgow, UK.

[5]Also supported by LPNHE, Universités de Paris VI et VII, Paris, France.

[6]Supported by the CERN Doctoral Student Programme.

[7]Now at Imperial College, University of London, UK.

[8]ITEP, Moscow, Russian Federation.

[9]Permanently at Instituto de Física de Cantabria, Univ. de Cantabria, Santander, Spain.

[10]Now at SpinX Technologies, Geneva, Switzerland.

[11]Now at TRIUMF, Vancouver, Canada.

[12]Now at University of St. Gallen, Switzerland.

[13]On leave of absence from Ecoanalitica, Moscow State University, Moscow, Russia.

[14]Now at Çukurova University, Adana, Turkey.

[15]Now at III Phys. Inst. B, RWTH Aachen, Aachen, Germany.

[16]On leave of absence from INFN, Sezione di Ferrara, Italy.

[17]Now at CERN, Geneva, Switzerland.

[18]Now at Univerity of Rome Tor Vergata, Italy.

[19]Now at Lawrence Berkeley National Laboratory, Berkeley, California, USA.

[20]K2K Collaboration.

[21]MiniBooNE Collaboration.

[22]Now at Section de Physique, Université de Genève, Switzerland, Switzerland.

[23]Now at Royal Holloway, University of London, UK.

[24]Now at University of Sussex, Brighton, UK.

[25]Now at ESA/ESTEC, Noordwijk, The Netherlands.

1 Introduction

The HARP experiment was designed to make measurements of hadron yields from a large range of nuclear targets and for incident particle momenta from 1.5 GeV/c – 15 GeV/c. Among its primary goals were to contribute in a fundamental way to the detailed understanding of neutrino beams of several experiments, among them:

- The K2K experiment, which has recently published its final results [1] confirming the evidence of atmospheric oscillations observed by Super-Kamiokande [2].

- The MiniBooNE experiment [3], whose results will confirm or exclude the evidence of neutrino oscillations observed by the LSND experiment [4].

- A new application of HARP data arises after the recent approval of the SciBooNE experiment [7], which will take data in the same neutrino beam used by MiniBooNE in order to perform a precision measurement of neutrino cross sections in the energy region around 1 GeV.

The calculation of the flux and relative neutrino composition of a neutrino beam requires a precise measurement of the interaction cross-section between the beam particles and the target material. In the case of the K2K and MiniBooNE/SciBooNE experiments, the dominant component of the beam (muon neutrinos) comes from the decay of positive pions produced in the collisions of incident protons on a nuclear target. To compute the ν_μ flux one needs a 4π parameterization of the differential cross section, $d^2\sigma^{\pi^+}/dpd\Omega$, which, in order to be reliable, must be based on a wide-acceptance, precise measurement.

The physics program of the HARP experiment includes the calculation of those cross-sections, taking advantage of the excellent features of its forward spectrometer (see [5] for a detailed description), namely: a very large angular and momentum acceptance, good resolution and excellent particle identification (PID) over the whole range of interest. Fig. 1 shows a schematic of the HARP detector. Five modules of the NOMAD drift chambers [6] (NDC1-5) and the dipole magnet comprise the forward spectrometer; a time-of-flight wall (TOFW), Cherenkov detector (CHE) and electromagnetic calorimeter (ECAL) make up the particle identification system.

An earlier publication reported measurements of the π^+ cross-sections from an aluminum target at 12.9 GeV/c [8]. This corresponds to the energies of the KEK PS and the target used by the K2K experiment. The results obtained in [8] were subsequently applied to the final neutrino oscillation analysis of K2K [1], allowing a significant reduction of the systematic error associated with the calculation of the K2K far-to-near ratio (see [8] and [1] for a detailed discussion) and thus an increased sensitivity to the oscillation signal.

Our next goal is to contribute to the understanding of the MiniBooNE and SciBooNE neutrino fluxes. They are both produced by the Booster Neutrino Beam at Fermilab which originates from protons accelerated to 8.9 GeV/c by the Fermilab booster before being collided against a beryllium target. As was the case for the K2K beam, a fundamental input for the calculation of the resulting ν_μ flux is the measurement of the π^+ cross-sections from a beryllium target at 8.9 GeV/c, which will be presented in this paper.

Further improvements to the understanding of the neutrino beams of K2K and MiniBooNE/SciBooNE (including the measurement of negative pion yields, kaon yields and the effect of a thick target) will follow in subsequent publications.

With respect to our previously published paper, we also present here a number of significant improvements to the analysis techniques and detector simulation. The most important improvements introduced in this analysis compared with the one presented in [8] are:
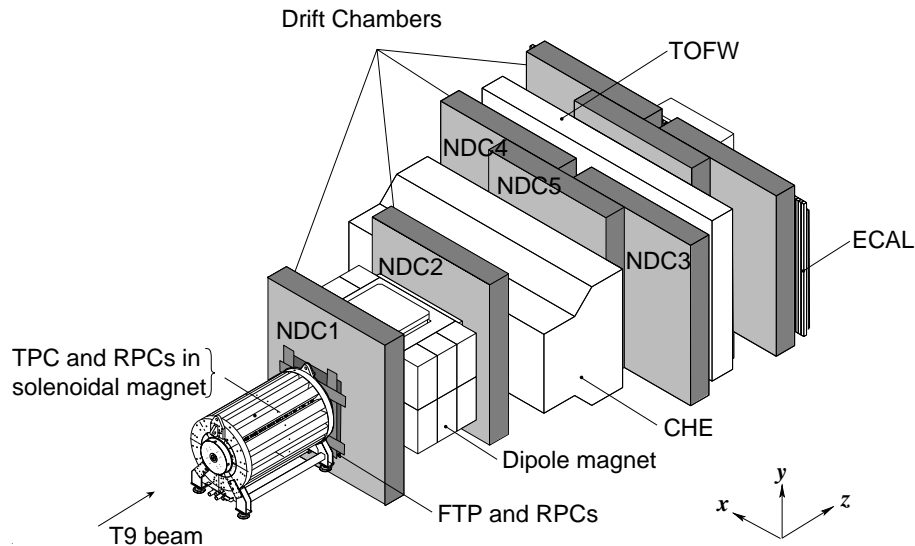
Figure 1: Schematic layout of the HARP spectrometer. The convention for the coordinate system is shown in the lower-right corner. The three most downstream (unlabeled) drift chamber modules are only partly equipped with electronics and not used for tracking.

- An increase and smoothing of the track reconstruction efficiency and better momentum resolution coming from an improvement in the tracking algorithm.

- Better understanding of the momentum scale and resolution of the detector, based on data which was then used to tune the simulation. This results in smaller systematic errors associated with the unsmearing factor determined from Monte Carlo.

- New particle-ID hit selection both in TOFW and in CHE resulting in much reduced background and negligible efficiency losses.

- Significant increases in Monte Carlo production have reduced uncertainties from Monte Carlo statistics and allowed studies which have reduced certain systematics.

We point out that an analysis incorporating these improvements yields results for the aluminum data fully consistent with those published in [8].

This paper is organized as follows. In section 2 we summarize the calculation of the cross-section. Track selection and the necessary corrections to the resulting yields are discussed in section 3. The determination of the momentum scale and the corrections associated with momentum resolution are discussed in section 4. In section 5 we describe our particle identification, an area where sizable improvement has been achieved since our first publication. Physics results are presented in section 6 and the impact of these to the MiniBooNE experiment is illustrated in section 7. The conclusions are presented in section 8.

2   Calculation of the double-differential inelastic cross-section

The goal of this analysis is to measure the inclusive yield of positive pions from proton-beryllium collisions at 8.9 GeV/c,

$$\mathrm{p} + \mathrm{Be} \rightarrow \pi^+ + X \ .$$

The absolutely normalized double-differential cross-section for this process can be expressed in bins of pion kinematic variables in the laboratory frame, (p_π, θ_π), as

$$\frac{d^2\sigma^{\pi^+}}{dpd\Omega}(p_\pi, \theta_\pi) = \frac{A}{N_A \rho t} \cdot \frac{1}{\Delta p \Delta\Omega} \cdot \frac{1}{N_{\text{pot}}} \cdot N^{\pi^+}(p_\pi, \theta_\pi) \ , \tag{1}$$

where:

- $\frac{d^2\sigma^{\pi^+}}{dpd\Omega}$ is the cross-section in $\text{cm}^2/(\text{GeV}/c)/\text{srad}$ for each (p_π, θ_π) bin covered in the analysis

- $\frac{A}{N_A \rho}$ is the reciprocal of the number density of target nuclei for beryllium ($1.2349 \cdot 10^{23}$ per cm^3).

- t is the thickness of the beryllium target along the beam direction. The thickness is measured to be 2.046 cm with a maximum variation of 0.002 cm.

- Δp and $\Delta\Omega$ are the bin sizes in momentum and solid angle, respectively.[1]

- N_{pot} is the number of protons on target after event selection cuts (see section 3.1).

- $N^{\pi^+}(p_\pi, \theta_\pi)$ is the yield of positive pions in bins of true momentum and angle in the laboratory frame.

In practice the full yields are not measured directly in bins of true kinematic quantities. There are particles which do not create reconstructible tracks in the detector and measurement resolutions which must be considered. Thus a set of corrections and unsmearing matrices must be applied to the measured yields. In addition, there is a small but non-negligible mis-identification of particle types, predominantly between pions and protons. Therefore, both yields must be measured simultaneously in order to correct for migrations. Eq. 1 can be generalized to give the inclusive cross-section for a particle of type α

$$\frac{d^2\sigma^\alpha}{dpd\Omega}(p, \theta) = \frac{A}{N_A \rho t} \cdot \frac{1}{\Delta p \Delta\Omega} \cdot \frac{1}{N_{\text{pot}}} \cdot M^{-1}_{p\theta\alpha p'\theta'\alpha'} \cdot N^{\alpha'}(p', \theta') \ , \tag{2}$$

where reconstructed quantities are marked with a prime and $M^{-1}_{p\theta\alpha p'\theta'\alpha'}$ is the inverse of a matrix which fully describes the migrations between bins of true and reconstructed quantities, namely: lab frame momentum, p, lab frame angle, θ, and particle type, α. In practice, the matrix M can be factorized into a set of individual corrections, as will be done here. The reasons for doing this are threefold:

- Not all efficiencies and migrations are functions of all three variables. Some, for example, are the same for pions and protons. Others do not depend on the angle.

- Using techniques described below the magnitude of many of the corrections can be determined from the data themselves, and do not rely on simulation. This is, of course, preferable wherever possible.

- Measuring and applying the corrections separately will ease the assessment of systematic errors as will be discussed in Section 6.

The form of the corrections can be separated into two basic categories: absolute efficiencies and bin–to–bin migrations between true and reconstructed quantities. In particular, migrations in momentum and in particle identification are carefully considered. The various efficiency corrections can, therefore, be functions of either reconstructed quantities or true ones, and must then be applied at the appropriate point in the analysis. This is important given that some corrections, as mentioned above, are measured from the data themselves where one has only reconstructed quantities. In the present analysis, $M^{-1}_{p\theta\alpha p'\theta'\alpha'}$ has been factorized into the following components:

---

[1] $\Delta p = p_{max} - p_{min}; \ \Delta\Omega = 2\pi(cos(\theta_{min}) - cos(\theta_{max}))$

- $\varepsilon^{\mathrm{recon}}(p^{'}, \theta^{'}_x, \theta^{'}_y)$ is the efficiency for the reconstruction of an 'analysis track'. An 'analysis track' is defined to include a momentum measurement as well as a matched time-of-flight hit needed for particle identification.

- $\varepsilon^{\mathrm{acc}}(\theta^{'})$ is the correction for the geometric acceptance of the spectrometer and is a purely analytical function based on the assumption of ϕ symmetry in hadron production and the fiducial cuts used in the analysis. See [8] for a full description of the acceptance correction and its dependence on the θ_y fiducial volume cut.

- $M_{pp'}^{-1}(\theta^{'})$ is the matrix describing the migration between bins of measured and true momentum. There is a separate matrix for each angular bin in the analysis since the momentum resolution and bias may vary with angle.

- $M_{\theta\theta'}^{-1}(p)$ is a unit matrix, implying that angular migrations, which are small, are being neglected.

- $\varepsilon^{\mathrm{absorb}}(p, \theta_x, \theta_y, \alpha)$ corrects for the absorption and decay of secondary particles before reaching the time-of-flight wall which is required for particle identification.

- $(1 - \eta^{\mathrm{tert}}(p^{'}, \theta^{'}_x, \theta^{'}_y, \alpha))$ corrects for the fraction η^{tert} of reconstructed analysis tracks which do not come from primary interactions of beam protons within the target, but rather from secondary interactions occurring elsewhere.

- $\varepsilon^{\mathrm{e\text{-}veto}}(p, \alpha)$ is the efficiency for particles of type α passing the electron veto cut used to remove electrons from the 'analysis track' sample as described below.

- $M_{\alpha\alpha'}^{-1}(p)$ is the particle identification efficiency and migration matrix, assumed uniform in θ.

Once again primed variables are those measured and unprimed variables are the true quantities (i.e. after unsmearing). $\theta_x = \tan^{-1}(p_x/p_z)$ and $\theta_y = \tan^{-1}(p_y/p_z)$ are useful variables for viewing the detector in roughly Cartesian coordinates and are related to the standard polar angle by $\theta = \tan^{-1}(\sqrt{\tan^2\theta_x + \tan^2\theta_y})$. Expanding $M_{p\theta\alpha p'\theta'\alpha'}^{-1}$ into these individual corrections and taking care of the order in which they are applied gives us the final equation for calculating the absolute cross-section from the measured yields.

$$
\begin{aligned}
\frac{d^2\sigma^\alpha}{dpd\Omega}(p,\theta) = & \frac{A}{N_{\mathrm{A}}\rho t} \cdot \frac{1}{\Delta p \Delta \Omega} \cdot \frac{1}{N_{\mathrm{pot}}} \\
& \times M_{\alpha\alpha'}^{-1}(p) \cdot \frac{1}{\varepsilon^{\mathrm{e\text{-}veto}}(p,\alpha)} \cdot \frac{1}{\varepsilon^{\mathrm{absorb}}(p,\theta_x,\theta_y,\alpha)} \\
& \cdot M_{pp'}^{-1}(\theta^{'}) \cdot (1 - \eta^{\mathrm{tert}}(p^{'}, \theta^{'}_x, \theta^{'}_y, \alpha)) \cdot \frac{1}{\varepsilon^{\mathrm{acc}}(\theta^{'})} \cdot \frac{1}{\varepsilon^{\mathrm{recon}}(p^{'}, \theta^{'}_x, \theta^{'}_y)} \\
& \cdot N^{\alpha'}(p^{'}, \theta^{'}) \,.
\end{aligned}
\tag{3}
$$

There are two additional aspects of the analysis methods which are worth mentioning. First, particle distributions are built by multiplying a set of correction weights for each reconstructed track and weighting events before they are added to the total yields. In this way a single reconstructed track is 'spread' over multiple true momentum bins according to the elements of $M_{pp'}^{-1}(\theta^{'})$, and the population in each true bin is comprised of tracks from all reconstructed momentum bins. This approach avoids the difficulties associated with inverting a large smearing matrix due to potential singularity of the matrix as well as potential pathologies in the inverted matrix caused by a loss of information at the kinematic boundaries of the matrix itself. The drawback to this method is that one has some sensitivity to the underlying spectrum in the Monte Carlo used to generate the matrix. A systematic error will be estimated to cover this dependence.

Second, there is a background associated with beam protons interacting in materials other than the nuclear target (parts of the detector, air, etc.). These events can be subtracted by using data collected without the nuclear target in place where one has been careful to normalize the sets to the same number of protons on target. We refer to this as the 'empty target subtraction':

$$N^{\alpha'}(p',\theta') \rightarrow [N^{\alpha'}_{\text{target}}(p',\theta') - N^{\alpha'}_{\text{empty}}(p',\theta')] \ .$$

The final form of the cross-section calculation is then given by making the above substitution into Eq. 3.

3   Track selection

3.1   Event selection

A good event is required to have a single, well reconstructed and identified beam particle from the T9 beam impinging on the nuclear target. A downstream trigger in the forward trigger plane (FTP) is also required to record the event, necessitating an additional set of unbiased, pre-scaled triggers for absolute normalization of the cross-section. These pre-scale triggers (1/64 for the 8.9 GeV/c Be data set) are subject to exactly the same selection criteria for a 'good' beam particle as the event triggers allowing the efficiencies of the selection to cancel, thus adding no additional systematic uncertainty to the absolute normalization of the result.

Beam protons are selected in the 8.9 GeV/c data set exactly as in the 12.9 GeV/c data set and as described in reference [8]. Two threshold Cherenkov detectors (BCA and BCB) placed in the beam line are used to select protons by requiring no signal in either detector. The pulse height distributions for the 8.9 GeV/c beryllium data set are shown in Fig. 2. Protons were selected by requiring a pulse height less than 120 counts in both detectors. Fig. 3 shows the time-of-flight distributions of those beam tracks identified as protons and pions by the Cherenkov selection.[2] We see that the two time peaks are consistent with the proton and pion hypotheses.

Four multi-wire proportional chambers are also located in the primary beam line and used to determine the impact position and angle of the beam particle on the target. The full set of criteria for selecting beam protons for the analysis are as follows.

- pulse height corresponding to a recorded ADC-count less than 120 in both beam Cherenkov A and beam Cherenkov B.

- adequate time measurements in TOFA, TOFB and/or TDS for calculating an arrival time at the target (with the criteria described in Ref. [8]).

- extrapolated position at the target within a 10 mm radius of the center of the target.

- extrapolated angle at the target less than 5 mrad.

Applying these criteria we are left with the event totals summarized in Table 1.

---

[2]The beam time of flight system is made of two identical scintillator hodoscopes, TOFA and TOFB, recuperated from the previous NA52 experiment and a small target-defining trigger counter (TDS).
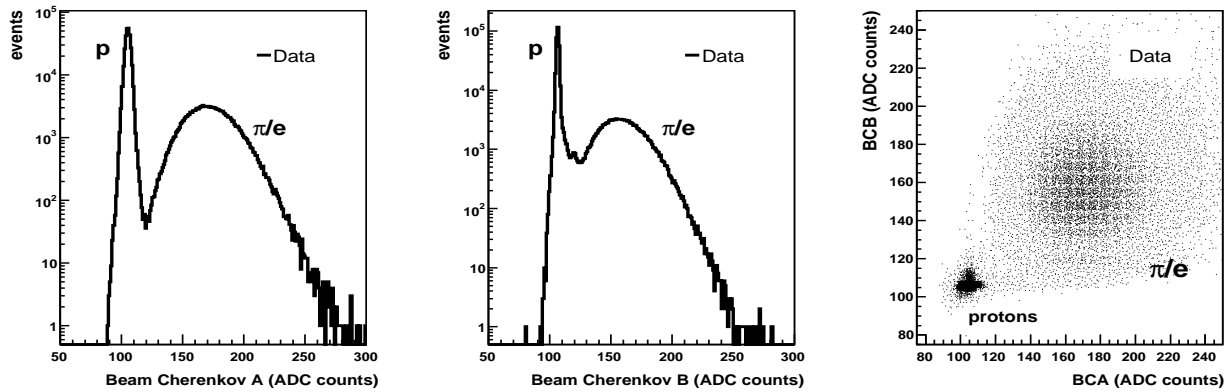
Figure 2: Beam Cherenkov pulse height distributions. BCA in the left panel, BCB in the middle, and BCB *vs.* BCA in the right panel. The electron and pion tagging efficiency is found to be close to 100%; the peaks are separated by $\approx 3\sigma$ in both detectors. By requiring a value compatible with a pedestal in both Cherenkov detectors the beam protons are clearly separable from pions and electrons as seen in the right panel.
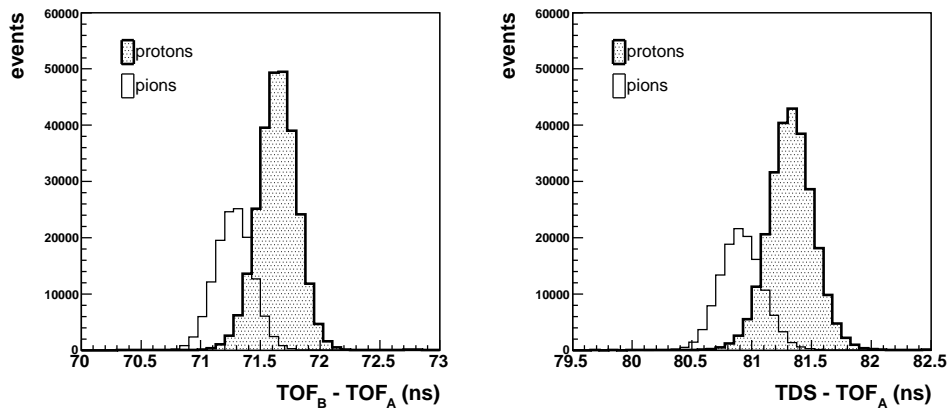

Figure 3: Beam time-of-flight distributions. The time difference between TOFA and TOFB is shown in the left panel. The right panel is the time difference between TOFA and the TDS. The hatched distributions are for particles identified as protons by the Cherenkov detectors as described in the text. The open histograms are all other beam tracks: pions, electrons and muons from pion decays.

3.2   Track selection

Secondary track selection criteria have been optimized to ensure the quality of the momentum reconstruction as well as a clean time-of-flight measurement while maintaining a high reconstruction efficiency. The following criteria have been applied to select tracks in the accepted events:

- a successful momentum reconstruction using downstream track segments in NDC modules 2,3,4 or 5 and the position of the beam particle at the target as an upstream constraint (here, *up*stream and *down*stream are relative to the spectrometer magnet);

- a reconstructed vertex radius (*i.e.* the distance of the reconstructed track from the *z*-axis in a plane

Table 1: Total number of events in the 8.9 GeV/c beryllium 5% λ_I target and empty target data sets, and the number of protons on target as calculated from the prescaled trigger count.

Data Set	Be 5% 8.9 GeV/c	8.9 GeV/c Empty Target
protons on target	13,074,880	1,990,400
total events processed	4,682,911	413,095
events with accepted beam proton	2,277,657	200,310
beam proton events with FTP trigger	1,518,683	91,690
total good tracks in fiducial volume	95,897	3,110

    perpendicular to this axis at $z = 0$) $r \ \leq 200$ mm;

- number of hits in the road around the track in NDC1 ≥ 4 and average χ^2 for these hits with respect to the track in NDC1 ≤ 30 (this is applied to reduce non-target interaction backgrounds);

- number of hits in the road around the track in NDC2 ≥ 6 (this is applied to reduce non-target interaction backgrounds);

- a matched TOFW hit passing the quality cuts described in Sec. 5.1.1;

- reconstructed angles are within the fiducial volume to be used for this analysis, $-210 \leq \theta_x \leq 0$ mrad and -80 $\leq \theta_y \leq 80$ mrad.

Applying these cuts to reconstructed tracks in accepted events we are left with 95,897 total good tracks in the beryllium thin target data set as shown in Table 1. The efficiency loss attributed to this selection is carefully measured and accounted for as described in detail in Sec. 3.3.1 below.

3.3 Sources of tracking inefficiency

There are two separate sources of tracking inefficiency which are considered. The reason for separating them, as will be made clear, is the ability to calculate one from the data directly and the need to use the Monte Carlo for the other. The distinction is basically this: the efficiency for reconstructing the track including a time-of-flight hit *given that the particle traversed the entire detector* versus the fractional loss of particles created in the target *before traversing the entire detector due to absorption and decay.* The former can be computed from the data themselves, while the latter is taken from a Monte Carlo simulation.

3.3.1 Track reconstruction efficiency

The track reconstruction efficiency can be measured from the data by exploiting two facts as described fully in [8]; first, the redundancy of detectors downstream of the spectrometer magnet and, second, the multiple possibilities for an upstream constraint in the extraction of track parameters. The interaction vertex is well defined using the MWPC extrapolation of the beam particle and the fact that the target is only 20.46 mm in thickness. This acts as one possible constraint on the upstream track segment. The other independent upstream constraint comes from the forward drift chamber module, NDC1 in Fig. 1. Using pure samples of well reconstructed tracks of one type, one can measure the efficiency for the other reconstruction method. The

efficiency to reconstruct a track for a particle traversing the detector using the target constraint method is greater than 95% and very flat when geometric acceptance is accounted for, as seen in Fig. 4.

3.3.2 Absorption, decay and tertiary track corrections

In order to identify particles in the forward spectrometer, we require a reconstructed 3-momentum as well as an associated time-of-flight measurement. The quality criteria for a kinematic measurement and the associated inefficiencies are discussed in Sec. 3.2, and the selection of time-of-flight hits and its efficiency will be addressed in Sec. 5.1.1.

The correction for absorption and decay, however, refers to secondary particles emanating from the nuclear target that never make it to the time-of-flight wall for detection and possible identification. Figure 1 shows the location of the time-of-flight scintillator wall just beyond the 'back plane' of drift chamber modules NDC3, NDC4 and NDC5. Using the forward detector alone this correction is impossible to estimate from the data themselves. We use the Monte Carlo simulation to determine the size of the correction and the result is shown in Fig. 5. Note this is an upward adjustment to the raw yield measured and is represented by $\varepsilon^{absorb}(p, \theta_x, \theta_y, \alpha)$ in Eq. 3. The absorption (which includes decay) is a function of θ_x and θ_y because it depends on the amount and type of physical material a particle passes through, thus the geometry of the detector. It is a function of α because of the different interaction cross-sections and decay times of various hadrons. This correction is separated from the tertiary correction discussed below because it does not depend on event multiplicity, kinematics or other details of the hadron production model used in the simulation, but only the total interaction cross-sections which are significantly more certain.

The tertiary correction refers to the subtraction of reconstructed tracks which were produced by secondaries interacting in the detector and not in proton beryllium collisions. The tertiary subtraction includes muons created in decays which are falsely identified as pions nearly 100% of the time due to their high β. The correction is significantly smaller than the absorption correction (compare Figs. 5 and 6), but is less certain, so the contribution to the systematic error is non-negligible as will be discussed in Sec. 6.

4   Momentum resolution and scale corrections

Two important sources of uncertainty in the analysis are those associated with the determination of the absolute momentum scale and those connected to the migration of reconstructed tracks between kinematic bins due to the finite resolution of the reconstruction. In both cases, the HARP spectrometer provides ways to use the data to tune up the Monte Carlo used to compute the corrections.

Momentum unsmearing is performed in the analysis by using the Monte Carlo to generate a momentum migration matrix, $M_{pp'}^{-1}(\theta')$ which describes how a reconstructed momentum value is distributed across bins of true momentum. The accuracy of this migration matrix, which is generated from Monte Carlo samples, depends upon two factors – the similarity of the underlying hadron distributions to those in the data and the agreement between the resolutions of reconstructed quantities in the data and Monte Carlo relative to the true momenta. The former will be addressed as part of the error discussion in Sec. 6. The latter, the agreement between the resolutions of reconstructed quantities in data and Monte Carlo, can be studied in multiple ways. The challenge is to isolate a set of tracks in the data sample with a known momentum. Three methods have been developed providing information that has been used to tune the detector simulation and ultimately to estimate a systematic uncertainty due to momentum resolution and scale.
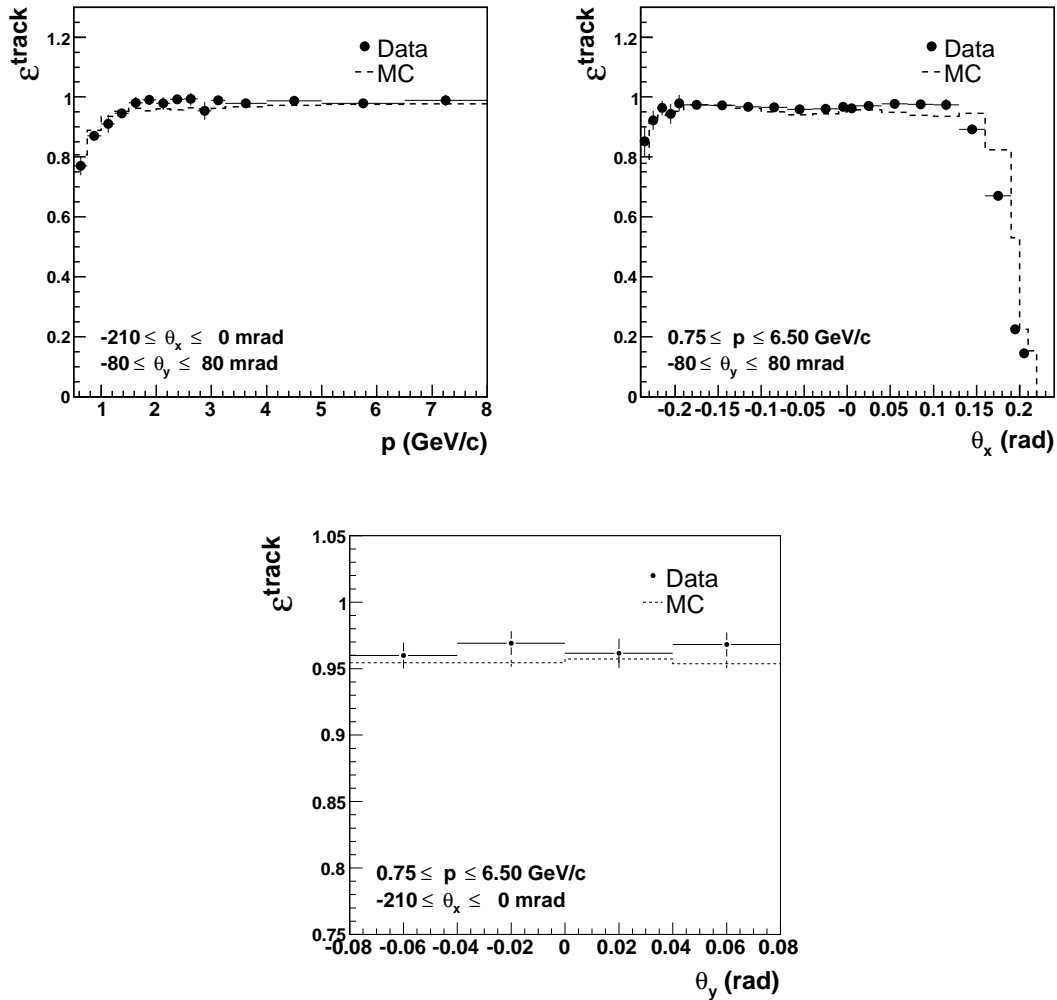
Figure 4: Tracking efficiency for positive particles traversing the detector using the target as upstream track constraint vs. particle momentum (upper left), production angle in the horizontal plane, θ_x (upper right), and production angle in the vertical plane, θ_y (lower). The drop in efficiency at low momentum is due to the requirement that the reconstructed vertex radius be less than 200 mm. The drop at large, positive values of θ_x is due to geometric acceptance as low momentum tracks are bent out of the spectrometer missing the downstream chambers. The present analysis is performed using tracks in the range $-0.210 \leq \theta_x \leq 0$ radians where the acceptance is flat in momentum. The θ_y plane is orthogonal to the spectrometer bending plane and therefore not sensitive to the momentum dependent acceptance. The θ_y efficiency, therefore, gives the purest measure of the average track reconstruction efficiency within the fiducial volume.
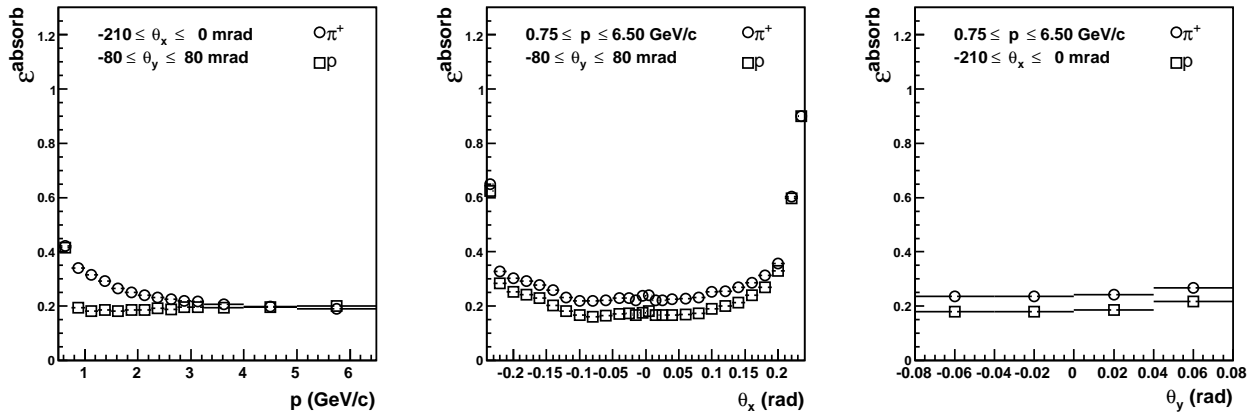
Figure 5: Absorption corrections for pions and protons according to Monte Carlo simulation vs. particle momentum (left), production angle in the horizontal plane, θ_x (center) and production angle in the vertical plane, θ_y (right). The 'absorption correction' also includes decay for pions.
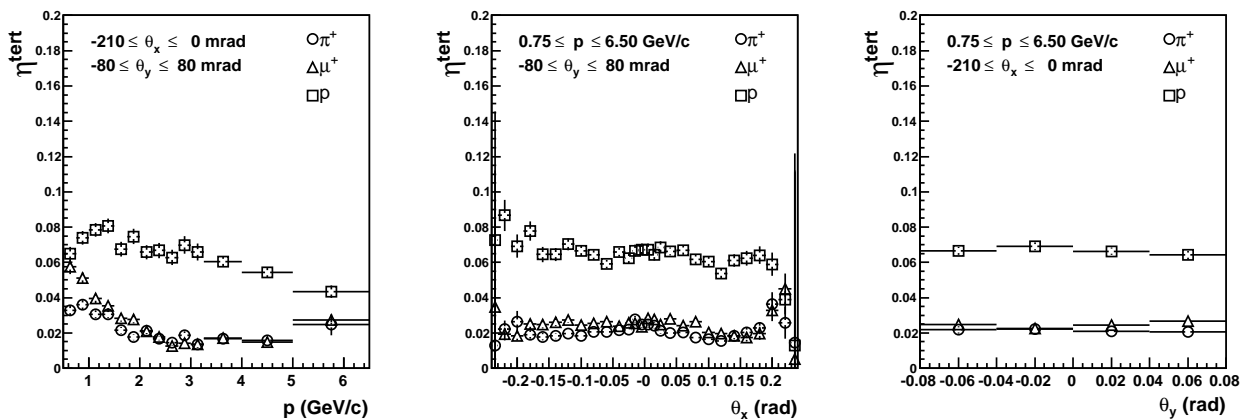

Figure 6: Tertiary particle rates for pions, muons (which get identified as pions) and protons according to Monte Carlo simulation vs. particle momentum (left), production angle in the horizontal plane, θ_x (center) and production angle in the vertical plane, θ_y (right).
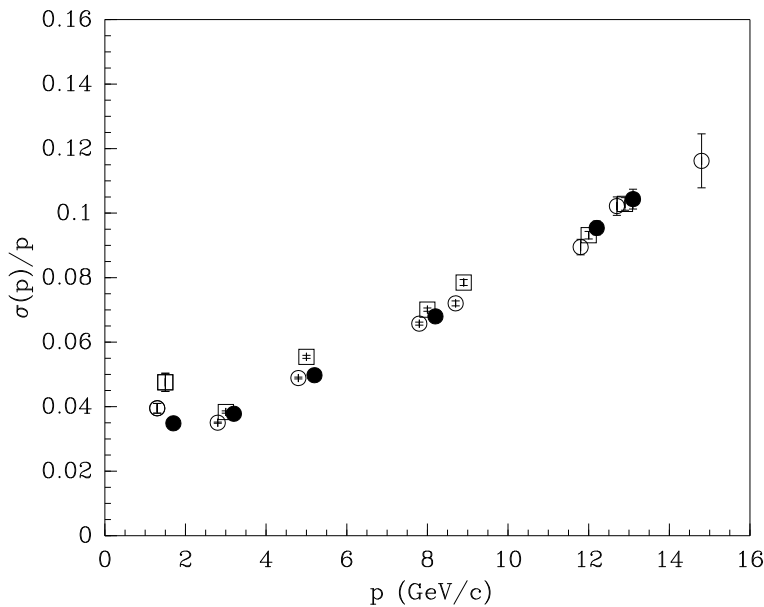
Figure 7: Momentum resolution $\sigma(p)/p$ (Gaussian fit) as a function of momentum (in GeV/c) for the drift chambers: the data were taken using several well-defined discrete beam momenta and no target for pions (open circles) and protons (open squares). Also shown (filled circles) is the corresponding resolution found using the Monte Carlo simulation.

4.1   Momentum calibration using empty target data sets

One method is to use empty target data sets where the incoming beam momentum value acts as the known momentum. Fig. 7 shows the result of such a study using empty target data and Monte Carlo samples for beam momenta of 1.5, 3.0, 5.0, 8.0, 8.9, 12.0, 12.9 and 15.0 GeV/c. The shape of the σ_p/p curve *vs.* momentum is as expected, and the agreement between data and Monte Carlo is excellent. For the previous analysis [8] only these 'test-beam data' were available, sampling the spectrometer response on the z-axis only. Now, additional methods have been used. A method using samples of elastic scattering events extends the range to larger angles while a method employing the time-of-flight detector covers the region of low momenta. Thus the full range of relevant angles and momenta is covered.

4.2   Momentum calibration using elastic scattering events

The elastic scattering process provides one track in the forward direction with a momentum close to the beam momentum and a soft large angle proton. In p–p and π–p scattering the kinematics is fully determined by the measurement of the direction of one of the outgoing particles. The precision of the measurement of the angle of the forward scattered particle is sufficient to predict the momentum of that particle without significant error. Elastic events can be readily selected by imposing combined criteria in the large angle and forward spectrometer. The main selection is the requirement of one and only one track in the TPC, identified as a proton, and exactly one track in the forward direction. Further constraints have been used, such as a match of the kinematics of these tracks and the selection of events with exactly the expected number of hits in the trigger counters and the barrel RPC detectors around the TPC. In these selections no constraints on the momentum measurement of the forward track has been set.

Figure 8 shows the results of an analysis of elastic events using 3 GeV/c, 5 GeV/c, and 8 GeV/c beams impinging
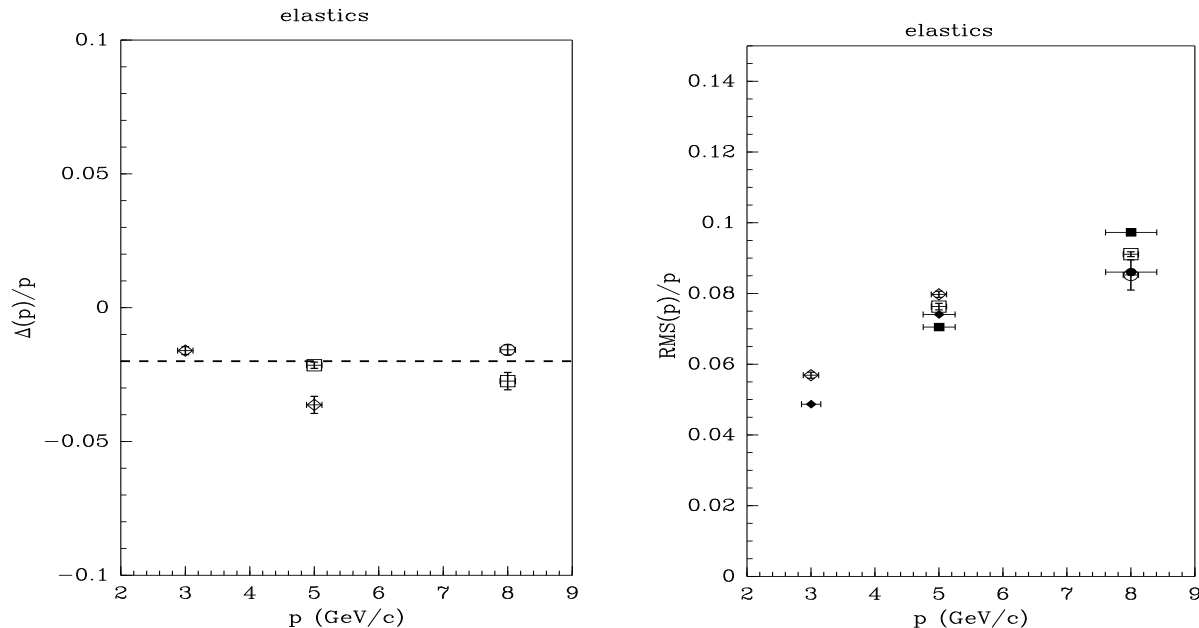
Figure 8: Momentum scale $\Delta(p)/p$ and resolution $\sigma(p)/p$ (Gaussian fit) as a function of momentum in two angular regions (circles: 30–60 mrad; boxes: 60–100 mrad). The data were taken using 3 GeV/c, 5 GeV/c and 8 GeV/c beams impinging on a hydrogen target. The left plot shows the momentum scale measured from data. The right plot shows the resolutions from data (open symbols) compared with the corresponding Monte Carlo simulations (filled symbols). Incoming pion and proton data are combined.

on a hydrogen target. Incoming pion and proton data are combined. The left panel reveals a momentum offset in the data of about 2% at all momenta and in two angular regions, 30-60 mrad and 60-100 mrad. This 2% will contribute a systematic uncertainty to the final cross-section and will be discussed in Sec. 6.1. The right panel shows the RMS of the momentum measurement as a function of momentum in the same two angular regions. The resolution measured from data is compared to that in the Monte Carlo and, as with the empty target samples, the agreement is excellent.

The momentum scale and resolution measured with the elastic events extends the calibration toward larger angles than probed with the empty target data alone and make it possible to characterize the spectrometer over a larger range of its aperture. However, the lowest momentum at which these data are available is 3 GeV/c, such that another method had to be developed to study the performance of the spectrometer for lower momentum particles.

4.3   Momentum calibration using time-of-flight

The TOFW system [10] can be used to provide a momentum calibration in a momentum range where the dependence of the time-of-flight on the momentum for pions is much smaller than for protons and at the same time the resolution of the TOFW is better than the prediction of β for protons based on the momentum measurement. For protons the sensitivity to the momentum resolution is larger than all other dependencies in the beta resolution in the region $0.22 \, \mathrm{GeV}/c < p < 2.0 \, \mathrm{GeV}/c$. The TOFW$\beta$ resolution is typically $\sigma(\beta)/\beta = 0.005$. The precision $\sigma(\beta_{\mathrm{pred}})/\beta$ in the calculation of β for protons ranges from 0.05 at 0.22 GeV/c to 0.005 at 2 GeV/c due to the momentum resolution which is of the order of 100 MeV/c in this range. Therefore the width of the β peak for a sample of protons selected in a small range in *measured momentum* shows a large sensitivity to the

momentum resolution.

To exploit this feature for the determination of the momentum resolution at small momenta the time-response of the TOFW has to be measured for pions and protons separately. First a very clean sample of pions is selected. Particles of negative charge are selected for this purpose to provide negative pions. In principle, this sample can be contaminated by electrons and negative kaons. Antiprotons are expected to be negligible. At a momentum below the Cherenkov threshold for pions, electrons are rejected by retaining only particles without a signal in the Cherenkov detector. The remaining sample contains mainly π^- with a small background of K^-. This kaon background is visible in the TOF spectrum and can be taken into account.

At a momentum above the pion Cherenkov threshold, the π^- sample is selected by requiring a signal in the Cherenkov. Although the electron background is expected to be small at these momenta, a selection with the calorimeter is used to reject them. The same selection is also used at momenta below Cherenkov threshold in addition to the rejection with the Cherenkov detector. Thus a sufficiently clean sample of negative pions can be obtained in the whole momentum range.

From the sample of positive particles, positrons are removed by the selection using the electron identifier. Below Cherenkov threshold only particles without signal in the Cherenkov are used. This selection retains protons, kaons and pions below pion Cherenkov threshold and only protons and kaons above the threshold. The precision of the TOFW is sufficient to provide a good separation of pions and protons below pion Cherenkov threshold. Thus, in the whole range relevant for the experiment a clean sample of protons can be obtained, albeit with a small contamination of kaons. As mentioned above, the measurement with the negative pions characterizes the TOFW response, both its absolute time and its time resolution. The negative pions also provide a perfect prediction for the behavior of the TOFW measurement for the positive pions.

The measurement of the properties of the momentum determination in the spectrometer is then obtained by selecting small regions (bins) of *measured* momentum and fitting the β spectrum of protons with a function which takes into account the width of the momentum bin, the calibrated β resolution and as free parameter the momentum resolution. The results for data and Monte Carlo and in four angular regions are shown in Fig. 9. The resolution measured should be interpreted as an RMS of the momentum resolution and is larger than the σ of the Gaussians fitted to the direct beam data using the runs without target, but consistent with the RMS of the latter.

Combining information from these three techniques one is able to map out the momentum resolution and scale in both data and Monte Carlo for comparison. The results indicate good agreement across a range of momenta and angles allowing us to utilize the Monte Carlo simulation to generate the momentum resolution correction matrix, $M_{pp'}^{-1}(\theta')$. However, a systematic uncertainty due to this method is considered and will be discussed below.

5   Particle identification

The present analysis uses particle identification information from the time-of-flight and Cherenkov PID systems; the discrimination power of time-of-flight below 3 GeV/c and the Cherenkov detector above 3 GeV/c are combined to provide powerful separation of pions and protons. The calorimeter is presently used only for separating pions and electrons when characterizing the response of the other detectors. The resulting efficiency and purity of pion identification in the analysis region is excellent.
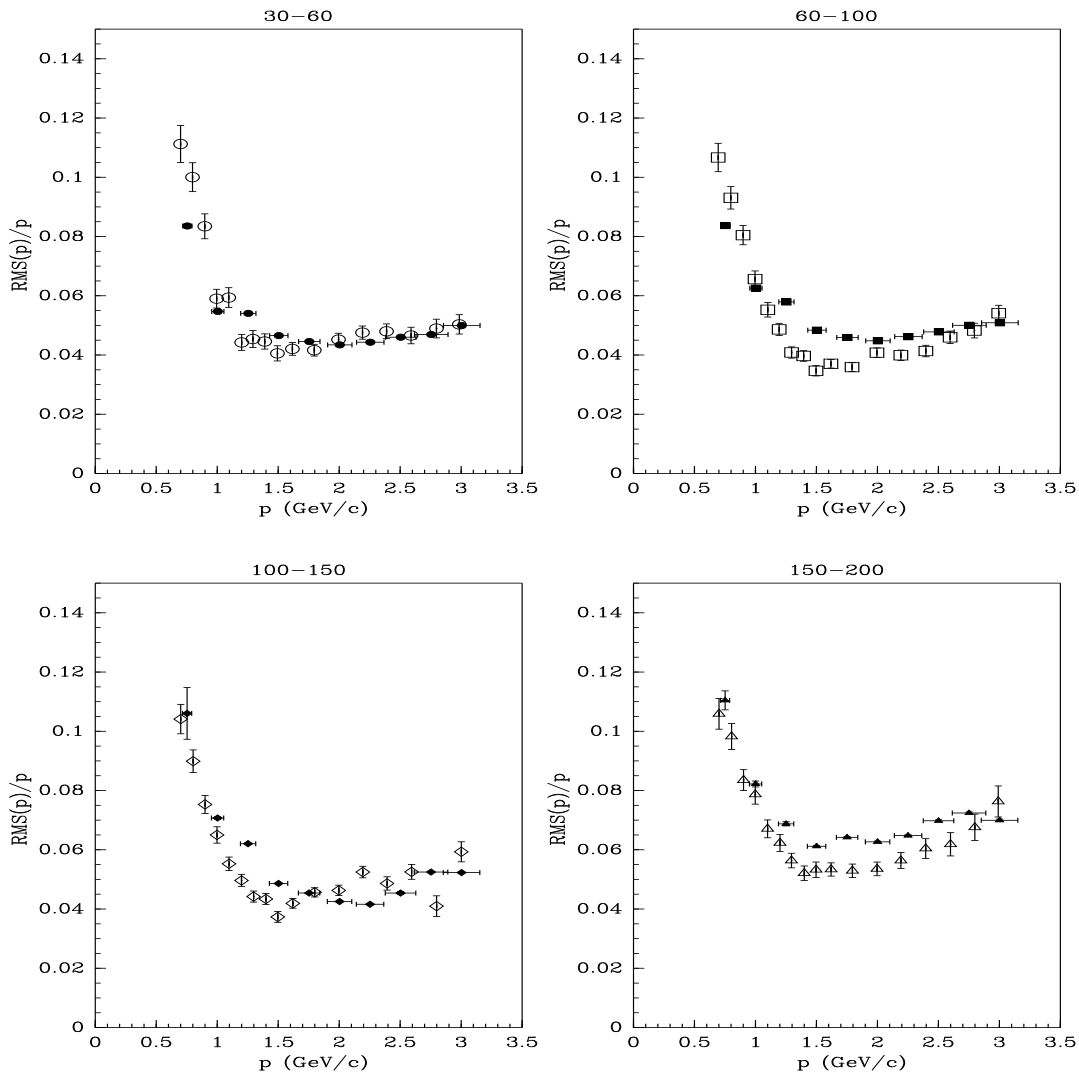
Figure 9: RMS momentum resolution as a function of momentum in four angular bins (circles: 30–60 mrad; boxes: 60–100 mrad; diamonds: 100–150 mrad; triangles: 150–200 mrad). Data are shown with open symbols; Monte Carlo with filled symbols.

Particle identification is performed by determining the probability that a given track is a pion or a proton based on the expected response of the detectors to each particle type (see below) and the measured response for the track. Information from both detectors is combined for maximum discrimination power using a Bayesian technique,

$$P(\alpha|\beta, N_{\mathrm{pe}}, p, \theta) = \frac{P(\beta, N_{\mathrm{pe}}|\alpha, p, \theta) \cdot P(\alpha|p, \theta)}{\sum\limits_{i=\pi, \mathrm{p}, \dots} P(\beta, N_{\mathrm{pe}}|i, p, \theta) \cdot P(i|p, \theta)} \ . \tag{4}$$

There are several simplifications that can immediately be applied to Eq. 4. First, we will assume no *a priori* knowledge of the underlying pion/proton spectra; that is the prior distributions will be flat and equal everywhere, $P(i|p, \theta) = 1$ for all p, θ. Second, we will consider the response functions of the different PID detectors as independent and can therefore factorize the probability into separate terms for each detector used. In addition, the time-of-flight and Cherenkov detector responses show no angular dependence allowing θ to be removed from

the above expression. Finally, we will only consider pions and protons as possible secondary particle types,

$$P(\alpha|\beta, N_{\mathrm{pe}}, p) = \frac{P(\beta|\alpha, p) \cdot P(N_{\mathrm{pe}}|\alpha, p)}{P(\beta, |\pi, p) \cdot P(N_{\mathrm{pe}}|\pi, p) + P(\beta|\mathrm{p}, p) \cdot P(N_{\mathrm{pe}}|\mathrm{p}, p)} \ . \tag{5}$$

From this equation a pion probability can be calculated. Pions are selected by making a cut in this probability variable, equal to 0.6 in the present analysis. The efficiency for pion selection and the migration between pions and protons can be calculated analytically from the detector response functions for a given cut in probability as discussed in Sec. 5.2.

5.1   PID detector hit selection and response functions

This section describes the quality criteria applied to PID detector hits which are used to identify reconstructed tracks. The reconstruction software associates any detector hit with any tracks where a geometric matching χ^2 is better than some maximum value. A Kalman filter package is used to extrapolate each track to the plane of the detector, and this position is compared to the reconstructed x, y position of all reconstructed hits in that detector. If the matching χ^2 is less than 30, then the hit is added to the candidates for that track. Further selection is done at the analysis stage and will be described below. Note that in this scheme the reconstruction can associate a single detector hit with multiple tracks and each track likely has multiple detector hits. These conflicts will be resolved by the selection outlined below.

5.1.1   Time-of-flight response

A good time-of-flight measurement is required for doing particle identification in this analysis. It was discovered, due to the presence of a significant, almost flat background far from the Gaussian peaks in the β distributions, that a more strict set of selection cuts was required to ensure a quality time-of-flight measurement. The small efficiency loss due to this selection can be measured directly from the data and will be combined with the tracking efficiency discussed above in an overall *reconstruction efficiency*,

$$\varepsilon^{recon} = \varepsilon^{track} \cdot \varepsilon^{TOFW-match} \ . \tag{6}$$

As mentioned above, each track can have multiple time-of-flight measurements ($TOFW - t_0$) associated with it coming out of the reconstruction. It is possible for a single hit to match up to multiple tracks if the tracks are close enough together when hitting the wall. It is also possible that electromagnetic showers associated with a particle passing through detector material can create additional hits beyond the primary hit caused by the hadron of interest. To minimize inaccurate time measurements due to these effects, the time-of-flight candidates for each track are time-ordered and the earliest hit passing the following criteria is selected:

- if the track shares the TOFW hit with another track, then it must have a better geometric matching χ^2;
- χ^2 match ≤ 6;
- total pulse-height from the two PMTs, $q_1 + q_2 \geq 1.5$.

The χ^2 distribution for track-TOFW hit matching and the total pulse-height distribution for this data set are shown in Fig. 10.

Having applied these criteria to time-of-flight measurements we must understand the associated efficiency loss as well as the remaining level of non-Gaussian component to the β spectrum. Each of these have been carefully measured and the needed corrections applied.
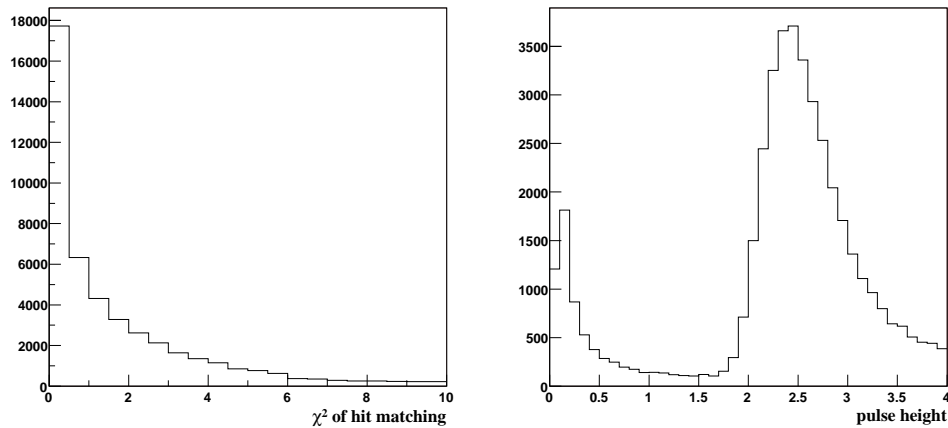
Figure 10: TOFW hit reconstructed variables. The left panel shows the distribution of the χ^2 between the extrapolated track position and the reconstructed scintillator hit position. The right panel shows the total PMT pulse height of the two PMTs ($q_1 + q_2$) on the scintillator volume that was hit. Time-of-flight hits are selected by requiring a $\chi^2 \leq 6$ and a combined pulse height, $q_1 + q_2 \geq 1.5$ (see the text).

The efficiency is measured from the data by using a clean sample of well reconstructed tracks which leave a signal in the calorimeter (downstream of the scintillator wall) and simply asking how often a quality time-of-flight measurement is found. Fig. 11 shows the matching efficiency for these cuts for both data and Monte Carlo. The efficiency is quite flat in momentum and on average around 94% in the data. This efficiency is combined with the tracking efficiency to provide the total analysis track reconstruction efficiency. The efficiencies generated from the data themselves have been used in the analysis for the results being presented here.

Having applied these selection criteria we must characterize the response of the time-of-flight detector for different particle types. The β response has been parameterized by a simple Gaussian function. In order to avoid any bias introduced by the simulation of the time-of-flight system a method has been developed to extract the response function directly from the data and has already been described in [8] and [9]. The result, and a comparison of the response extracted from data and Monte Carlo showing that any bias would have been small, is shown in Fig. 12. This Gaussian distribution is used to generate the probability value that will be used in Eq. 5.

Additionally, there is a small rate of non-Gaussian time-of-flight measurements, called "β-outliers", which must be accounted for separately. β-outliers are defined as time-of-flight measurements greater than 5σ from the mean of the expected β response function. This small, non-Gaussian part of the time-of-flight has been fully accounted for in the PID efficiency calculation to be described below. It should be noted that, due to the improvements in the hit selection criteria being described here, the β-outlier problem as described in [8] has been reduced from $\approx$10% to <1% since that publication and now makes a negligible contribution to the systematics in the cross-section analysis.

5.1.2   Cherenkov response

The Cherenkov detector is used to veto electrons below 3 GeV/c and to differentiate pions from protons above 3 GeV/c.

Below 3 GeV/c the Cherenkov signal is not used in the calculation of the particle identification probability
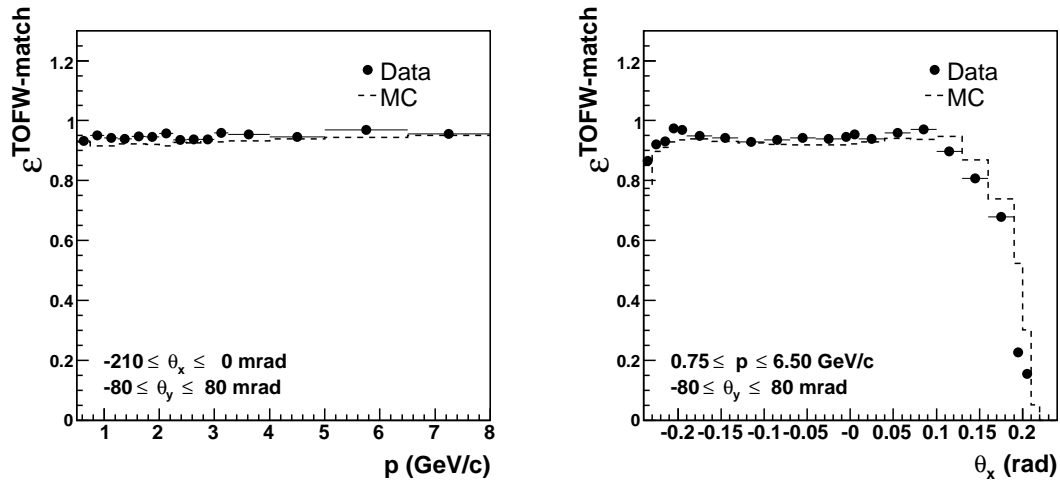
Figure 11: TOFW matching efficiency vs. particle momentum (left) and production angle in the horizontal plane, θ_x (right) as measured from data and Monte Carlo. The TOFW matching efficiency does not have the momentum dependence of the tracking efficiency, but does exhibit the same effects of geometric acceptance as the drift chambers as seen in the right, θ_x, plot. Note the present analysis is performed using tracks in the range $-0.210 \leq \theta_x \leq 0$ radians where the acceptance is flat in momentum.
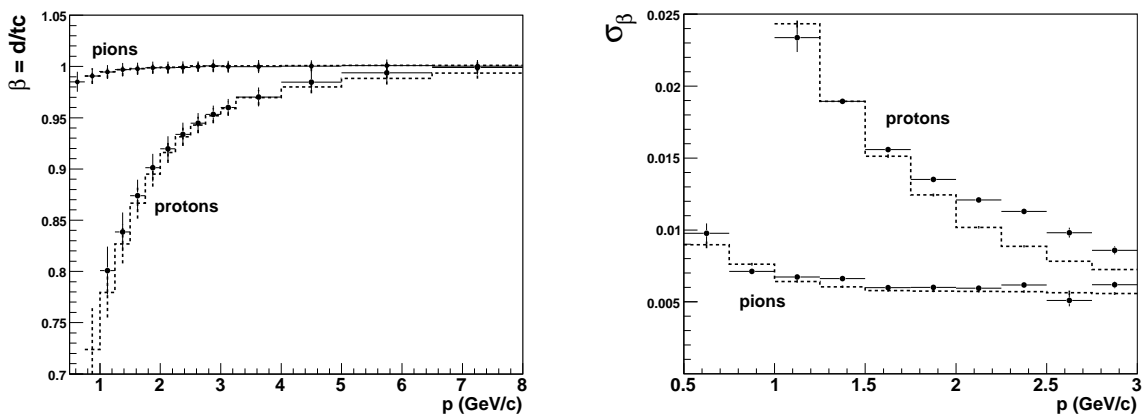

Figure 12: β response for pions and protons as measured from data and Monte Carlo. The left panel shows the mean beta values with the error bars representing the width of the Gaussian distribution. The right panel highlights the width of the distributions and shows how the resolution asymptotically approaches ≈ 0.006. The solid points are the response as measured from data; the dashed histograms are the response as measured from Monte Carlo.
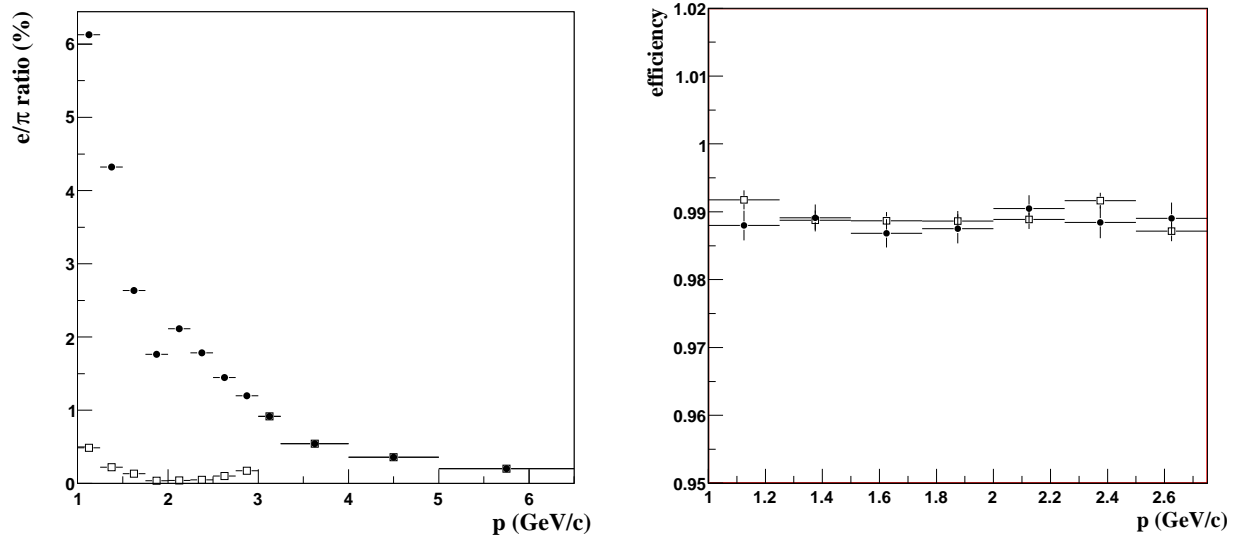
Figure 13: Electrons are removed from the sample by cutting tracks below 3 GeV/c with greater than 15 photo-electrons in the CHE. The left panel shows the e/π ratio from a Monte Carlo simulation before (solid points) and after (open squares) the application of a 15 photo-electron cut. This cut reduces the electron contamination to 0.5% or less in the region where it is applied. The right panel shows the efficiency for pions (solid points) and protons (open squares) to pass the 15 photo-electron cut below 3 GeV/c, and is $\approx$ 99% for both.

according to Eq. 5, but instead electrons are removed by a simple veto of tracks with greater than 15 photo-electrons. Fig. 13 demonstrates the effect of the electron veto cut. The left panel shows the e/π ratio in the Monte Carlo before and after applying the 15 photo-electron cut below 3 GeV/c. The remaining electron contamination is less than 1% everywhere, and less than 0.5% in the region where the veto is applied. One expects a very small efficiency loss for pions and protons due to this cut in photo-electrons and this is also shown in Fig. 13. Approximately 1% of pions and protons do not pass the electron veto; a correction has been applied in the present analysis. Future analyses of these and similar data will fully include information from the calorimeter making both this inefficiency and tiny impurity completely negligible.

Above 3 GeV/c the Cherenkov is a powerful discriminator of pions and protons. (Monte Carlo simulations indicate that there are a negligible number of electrons above 3 GeV/c and these are thus ignored.) Presently the Cherenkov is being used digitally. That is the spectral information of the light output is not being used. Instead we define a signal as an associated hit with greater than 2 photo-electrons. Two or less is considered no signal. Based on this definition we determine the efficiency for pions and protons to have a signal in the Cherenkov as a function of particle momentum. Fig. 14 shows the expected response for pions and protons in the Cherenkov both above and below the pion threshold. Above threshold the Cherenkov is greater than 99% efficienct for pions. The small efficiency for protons and pions below threshold of around 1.5% is due to false associations with light generated by other particles in the event.

5.2   Particle identification efficiencies and migrations

The method described in this section uses the measured response of the PID detectors and the definition of the pion–proton PID estimator to compute analytically the pion–proton PID corrections for a given cut on the PID
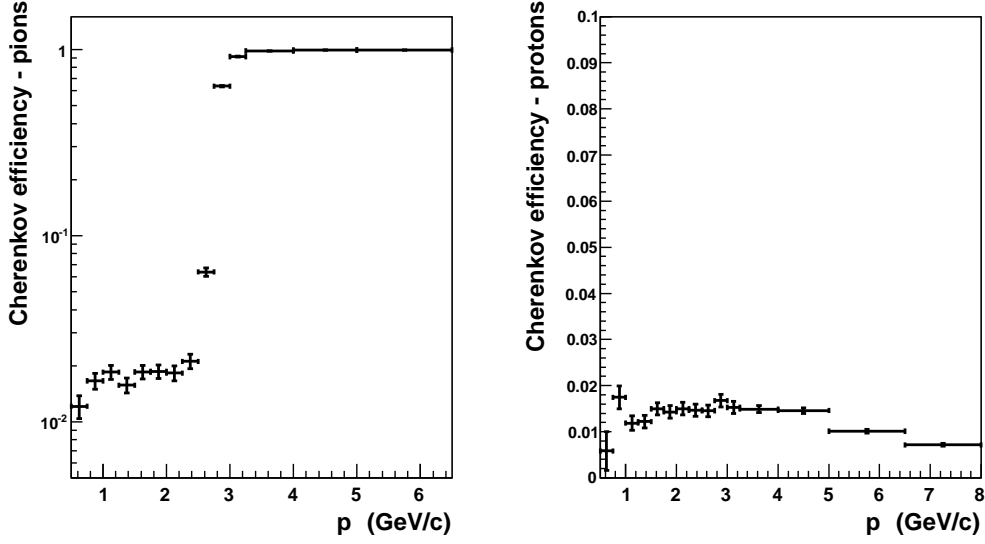
Figure 14: Cherenkov response for pions (left) and protons (right). The points are the efficiencies for a track to have an associated Cherenkov hit with greater than 2 photo-electrons. The threshold for pions at around 2.6 GeV/c is clearly visible (note the log scale). The small efficiency for protons and below threshold pions of around 1.5% is due to false associations with light genereted by other particles in the event.

estimator. These corrections consist (for each momentum bin) of a 2x2 matrix (PID efficiency matrix)

$$\begin{pmatrix} \pi \\ p \end{pmatrix}_{\text{rec}} = \begin{pmatrix} M_{\pi\pi} & M_{\pi p} \\ M_{p\pi} & M_{pp} \end{pmatrix} \cdot \begin{pmatrix} \pi \\ p \end{pmatrix}_{\text{true}} , \tag{7}$$

where $M_{\pi\pi}$ and M_{pp} are the efficiencies for correctly identifying pions and protons, respectively, and $M_{\pi p}$ and $M_{p\pi}$ are the migration terms of true protons identified as pions and true pions identified as protons, respectively. The full covariance matrix (16 terms) of the PID efficiency matrix is also computed analytically. This calculation is explained fully in [9]. The final expression for the PID efficiency–migration matrix elements reads:

$$M_{ij} = \sum_{S_c=0,1} C_j^{S_c} \cdot \left[\int_{\beta_\pi^{S_c},0}^{\infty,\beta_p^{S_c}} d\beta \; G_j(\beta) + \omega_j^{\pi p} \cdot S(P_i^{S_c}|_{\text{CHE}} > P_{\text{cut}}) \right] , \tag{8}$$

where $C_j^{S_c}$ is the Cherenkov efficiency shown in Fig. 14, $G_j(\beta)$ and $\omega_j^{\pi p}$ are the Gaussian and non-Gaussian contributions to the beta response, respectively, and $S(P_i^{S_c}|_{\text{CHE}} > P_{\text{cut}})$ is a step function controlling the integration of the non-Gaussian part, ω.

The 2x2 matrix of Eq. 7 is easily inverted for converting reconstructed yields into true yields of pions and protons. The elements of the matrix in Eq. 7 are shown in Fig. 15 as a function of particle momentum. The pion efficiencies are >95% and the migrations are all less than 1%.
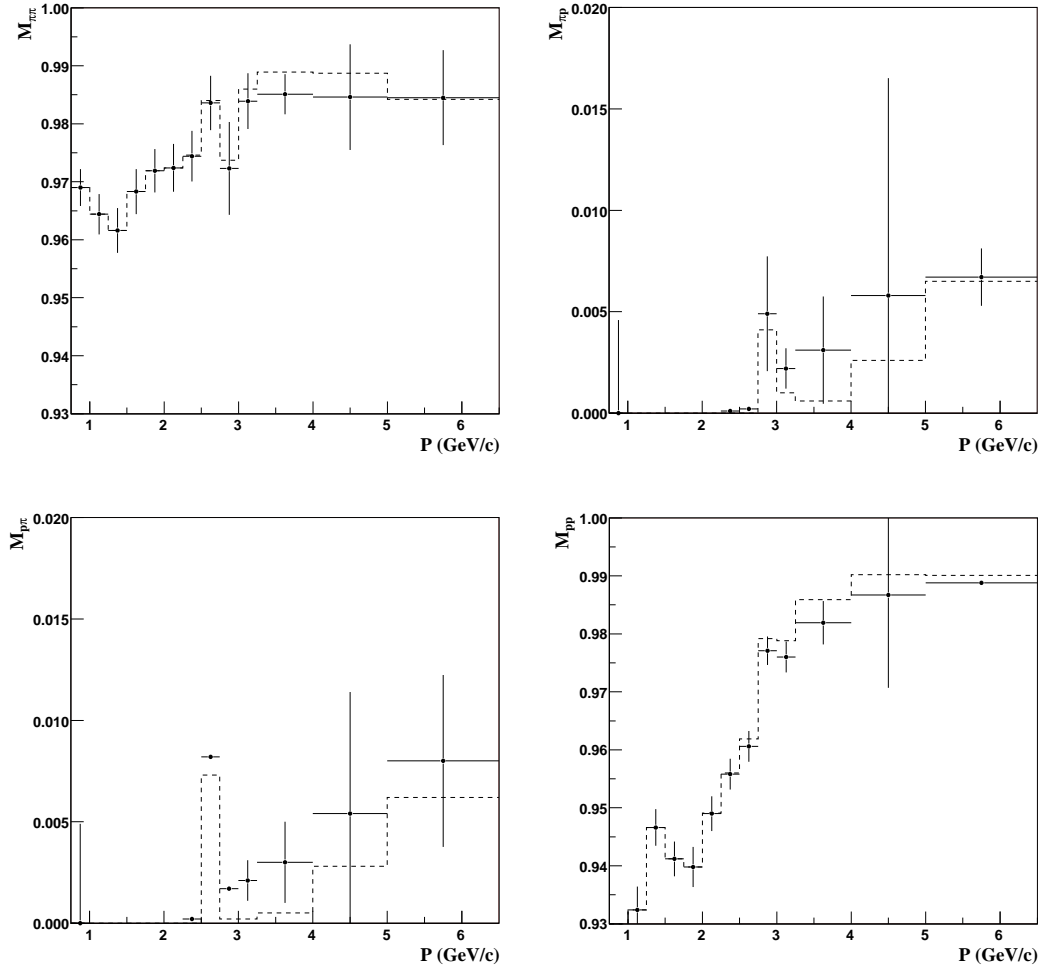
Figure 15: Particle ID efficiency and migration matrix elements as a function of momentum. Upper left is the pion identification efficiency, $M_{\pi\pi}$. Upper right is the proton to pion migration, $M_{\pi p}$. Lower left is the pion to proton migration, $M_{p\pi}$. Lower right is the proton identification efficiency, M_{pp}. Points with errors are the values calculated from data. The dotted hitograms are those determined from the Monte Carlo.

6 Physics results

Applying corrections to the raw yields as described in the previous sections and according to Eq. 3, we have calculated the double-differential inelastic cross-section for the production of positive pions from collisions of 8.9 GeV/c protons with beryllium in the kinematic range from 0.75 GeV/$c \leq p_\pi \leq$ 6.5 GeV/c and 0.030 rad $\leq \theta_\pi \leq$ 0.210 rad.

Systematic errors have been estimated and will be described below. A full $(13 \times 6)^2 = 6048$ element covariance matrix has been generated to describe the correlation among bins. The data are presented graphically as a function of momentum in 30 mrad bins in Fig. 16. The central values and square-root of the diagonal elements of the covariance matrix are listed in Table 5 in Appendix A.

6.1 Error estimation

A full systematic error evaluation has been performed on these data in order to estimate the accuracy of the measurement being presented. Statistical errors from both the beryllium target data and the 8.9 GeV/c empty target data set used to subtract non-target backgrounds are also included.

The uncertainties associated with the various corrections applied to convert measured yields into true cross-section results have been estimated through a combination of analytical and Monte Carlo techniques. The approach used here has largely followed the methods of [8].

Full correlations among different kinematic bins (p, θ) have been considered, but the 78×78 elements of the covariance matrix will not be published here. To characterize the uncertainties on this measurement we show the diagonal elements of the covariance matrix plotted on the data points in Fig. 16. Additionally, we define a dimensionless quantity, δ_{diff}, expressing the typical error on the double-differential cross-section

$$\delta_{\text{diff}} \equiv \frac{\sum_i (\delta[\Delta^2 \sigma^\pi / (\Delta p \Delta \Omega)])_i}{\sum_i (\Delta^2 \sigma^\pi / (\Delta p \Delta \Omega))_i} \ , \tag{9}$$

where i labels a given pion (p, θ) bin, $(\Delta^2 \sigma^\pi / (dp \cdot d\Omega))_i$ is the central value for the double-differential cross-section measurement in that bin, and $(\delta[\Delta^2 \sigma^\pi / (dp \cdot d\Omega)])_i$ is the error associated with this measurement. We also define the fractional error on the total integrated pion cross-section in the range of the measurement (0.75 GeV/$c \leq p < 6.5$ GeV/c, 30 mrad $\leq \theta < 210$ mrad), δ_{int}:

$$\delta_{\text{int}} \equiv \frac{\sqrt{\sum_{i,j} (\Delta p \Delta \Omega)_i C_{ij} (\Delta p \Delta \Omega)_j}}{\sum_i (\Delta^2 \sigma^\pi)_i} \ , \tag{10}$$

where $(\Delta^2 \sigma^\pi)_i$ is the double-differential cross-section in bin i, $(\Delta^2 \sigma^\pi / (\Delta p \Delta \Omega))_i$, multiplied by its corresponding phase space element $(\Delta p \Delta \Omega)_i$. C_{ij} is the covariance matrix evaluated for the double-differential cross-section data.

Table 2 summarizes these quantities for each of the various error sources considered with a typical total uncertainty of 9.8% on the double-differential cross-section values being reported and a 4.9% uncertainty on the total integrated cross-section.

Several improvements in the detector response understanding and in the cross-section analysis since our previous publication [8] allowed us to reduce the dominant systematic uncertainties affecting the measurement of the pion
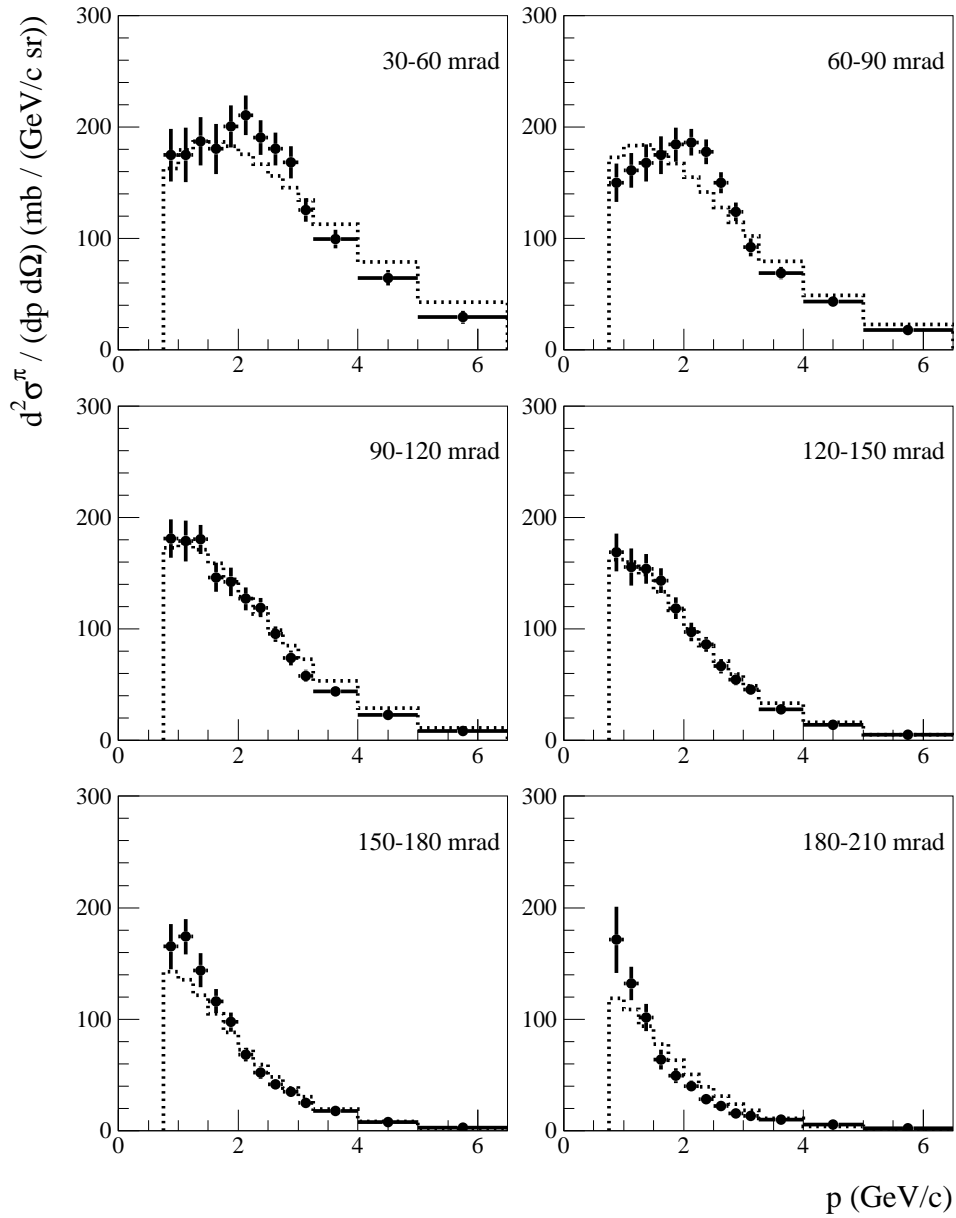
Figure 16: Measurement of the double-differential production cross-section of positive pions, $d^2\sigma^{\pi^+}/dpd\Omega$, from 8.9 GeV/$c$ protons on beryllium as a function of pion momentum, p, in bins of pion angle, θ, in the laboratory frame. The error bars shown include statistical errors and all (diagonal) systematic errors. The dotted histograms show the Sanford-Wang parametrization that best fits the HARP data.
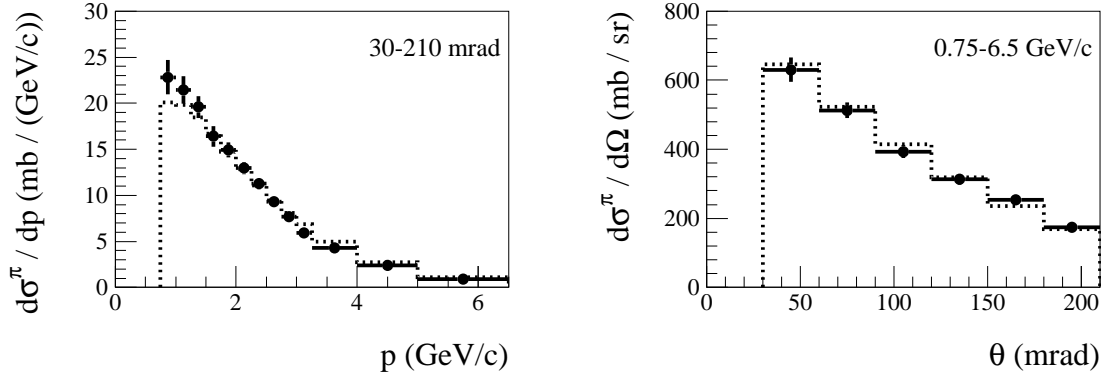
Figure 17: Projections of the double-differential cross-section results onto the momentum axis integrated over the angular range $30 \leq \theta < 210$ mrad (left) and onto the angle axis integrated over the momentum range $0.75 \leq p < 6.5$ GeV/c (right). Projections for the best-fit Sanford-Wang parametrization are also shown, as indicated by dotted histograms.

Table 2: Summary of the uncertainties affecting the double-differential cross-section (δ_{diff}) and integrated cross-section (δ_{int}) measurements. See text for details.

| Error Category	Error Source	$\delta^{\pi}_{\text{diff}}$ (%)	$\delta^{\pi}_{\text{int}}$ (%)
Statistical	Be target statistics	4.2	0.6
	Empty target subtraction (stat.)	4.6	0.6
	Sub-total	**6.3**	**0.8**
Track yield corrections	Reconstruction efficiency	1.3	0.8
	Pion, proton absorption	3.6	3.7
	Tertiary subtraction	1.8	1.8
	Empty target subtraction (syst.)	1.3	1.2
	Sub-total	**4.6**	**4.3**
Particle Identification	Electron veto	0.2	<0.1
	Pion, proton ID correction	0.4	0.1
	Sub-total	**0.5**	**0.1**
Momentum reconstruction	Momentum scale	3.6	0.1
	Momentum resolution	3.4	1.0
	Sub-total	**5.2**	**1.0**
Overall normalization	**Sub-total**	**2.0**	**2.0**
All	**Total**	**9.8**	**4.9**
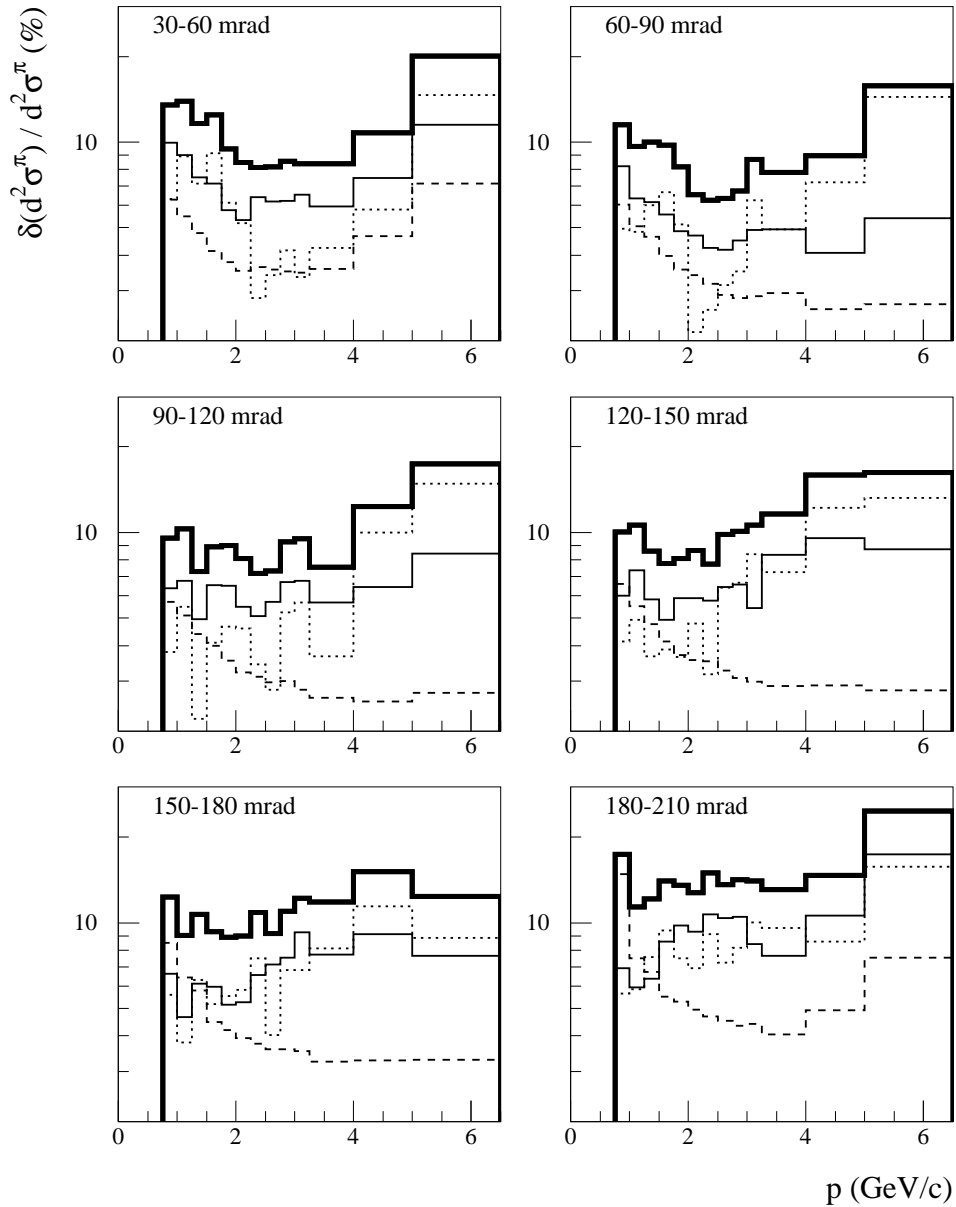
Figure 18: Fractional uncertainty (in percent) on the double-differential pion production cross-section measured, as a function of pion momentum and angle. The total uncertainty is shown by the thick black histograms, and individual contributions from the error categories given in Tab. 2 are also shown. Statistical, track yield corrections, and momentum reconstruction uncertainties are shown as thin solid, dashed, and dotted histograms, respectively; the overall normalization uncertainty is not shown, and the particle identification uncertainty contribution lies below 2% for all pion momenta and angles.

production cross-sections in the HARP spectrometer forward region. This also prompted us to release more spectral information in the pion cross-section measurement: 78 pion momentum/angle bins in this publication, instead of the 48 bins in [8] over the same pion phase space. With this new momentum binning the statistical and systematic uncertainties contribute approximately equally in most bins. The most significant improvements introduced in this analysis can be summarized as follows.

First, improvements in the TOFW and CHE hit association to tracks described in Section 5 translate into a negligible error contribution due to particle identification. Second, biases and accuracy for the momentum reconstruction algorithm have been studied in greater depth, as described in Section 4. This resulted in a better knowledge of the absolute momentum scale, now known to 2%, and of the momentum smearing caused by the HARP spectrometer, including our knowledge of the non-Gaussian contributions to the resolution function. Third, the study of HARP data samples other than the one described here allowed us to improve our understanding of low-energy hadronic interactions. We were able to validate our Monte Carlo-based correction to the pion cross-section due to the subtraction of tertiary tracks to within an uncertainty of 50%. Specifically, we have compared low energy p+C and π+C cross-sections to distributions from the Binary cascade [11] and Bertini intra-nuclear cascade [12] hadronic interaction models used to simulate the secondary interactions of p, n and $\pi^{\pm}$. The material in the HARP forward spectrometer where tertiary tracks might be produced is predominantely carbon. Fourth, better knowledge of proton beam targeting efficiency, and fully correlated contributions to track reconstruction and particle identification efficiencies, allowed us to reduce the normalization uncertainty on the pion cross-section measurement to 2%. In addition, increased statistics in the Monte Carlo samples used to correct for momentum unsmearing, absorption of secondary tracks and production of tertiary tracks, allowed us to reduce further the impact of Monte Carlo statistical uncertainties on the final cross-section results. These uncertainties have been taken into account in the results presented here, and have been shown to be negligible.

6.2   Sanford-Wang parametrization

Sanford and Wang [14] have developed an empirical parametrization for describing the production cross-sections of mesons in proton-nucleus interactions. This parametrization has the functional form:

$$\frac{d^2\sigma(\text{p+A} \rightarrow \pi^+ + X)}{dpd\Omega}(p,\theta) = \exp[A]p^{c_2}(1 - \frac{p}{p_{\text{beam}}}) , \tag{11}$$

where:

$$A = c_1 - c_3\frac{p^{c_4}}{p_{\text{beam}}^{c_5}} - c_6\theta(p - c_7p_{\text{beam}}\cos^{c_8}\theta) , \tag{12}$$

and X denotes any system of other particles in the final state, p_{beam} is the proton beam momentum in GeV/c, p and θ are the π^+ momentum and angle in units of GeV/c and radians, respectively, $d^2\sigma/(dpd\Omega)$ is expressed in units of mb/(GeV/c sr), $d\Omega \equiv 2\pi \ d(\cos\theta)$, and the parameters $c_1, \ldots, c_8$ are obtained from fits to meson production data.

The parameter c_1 is an overall normalization factor, the four parameters c_2, c_3, c_4, c_5 can be interpreted as describing the momentum distribution of the secondary pions, and the three parameters c_6, c_7, c_8 as describing the angular distribution for fixed secondary and proton beam momenta, p and p_{beam}.

The π^+ production data reported here have been fitted to this empirical formula. In the χ^2 minimization procedure, seven out of these eight parameters were allowed to vary. The parameter c_5 was fixed to the

Table 3: Sanford-Wang parameters and errors obtained by fitting the dataset. The errors refer to the 68.27% confidence level for seven parameters ($\Delta\chi^2 = 8.18$).

Parameter	Value
c_1	$(8.22 \pm 1.98) \cdot 10^1$
c_2	(6.47 ± 1.62)
c_3	$(9.06 \pm 2.03) \cdot 10^1$
$c_4 = c_5$	$(7.44 \pm 2.30) \cdot 10^{-2}$
c_6	(5.09 ± 0.49)
c_7	$(1.87 \pm 0.53) \cdot 10^{-1}$
c_8	$(4.28 \pm 1.36) \cdot 10^1$

Table 4: Correlation coefficients among the Sanford-Wang parameters, obtained by fitting the data.

Parameter	c_1	c_2	c_3	$c_4 = c_5$	c_6	c_7	c_8
c_1	1.000						
c_2	0.327	1.000					
c_3	0.986	0.482	1.000				
$c_4 = c_5$	-0.559	0.596	-0.411	1.000			
c_6	0.091	-0.467	-0.006	-0.545	1.000		
c_7	0.011	-0.101	-0.004	-0.129	0.234	1.000	
c_8	-0.080	0.411	0.006	0.471	-0.776	0.215	1.000

conventional value $c_5 \equiv c_4$, since the cross-section dependence on the proton beam momentum cannot be addressed by the present HARP data-set, which includes exclusively measurements taken at $p_{\text{beam}} = 8.9$ GeV/c. In the χ^2 minimization, the full error matrix was used.

Concerning the Sanford-Wang parameters estimation, the best-fit values of the Sanford-Wang parameters are reported in Table 3, together with their errors. The fit parameter errors are estimated by requiring $\Delta\chi^2 \equiv \chi^2 - \chi^2_{\text{min}} = 8.18$, corresponding to the 68.27% confidence level region for seven variable parameters. Significant correlations among fit parameters are found, as shown by the correlation matrix given in Table 4.

The HARP cross-section measurement is compared to the best-fit Sanford-Wang parametrization of Table 3 in Figs. 16 and 17. The goodness-of-fit of the Sanford-Wang parametrization hypothesis for the HARP results can be assessed by considering the best-fit χ^2 value of $\chi^2_{\text{min}} = 248$ for 71 degrees of freedom, indicating a very poor fit quality. Simply by looking at Fig. 16, it appears as if the Sanford-Wang parametrization were not able to model some of the data spectral features. Hints of similar spectral discrepancies may be found also in Ref. [8], in that case less obvious because of the coarser measurement binning. On the other hand, as already noted in [8], we remark that the goodness-of-fit depends on the correlations among the HARP cross-section uncertainties in different (p, θ) bins, and therefore cannot be inferred solely from Fig. 16. If these uncertainties were (incorrectly) treated as completely uncorrelated, the best-fit χ^2 value would decrease from 248 to 160. We defer to a later HARP publication, which should include a more comprehensive study of π^+ production at various beam momenta and from various nuclear targets, a more complete discussion on the adequacy of parametrization-driven models such as Sanford-Wang to describe HARP hadron production data.

7   Relevance of HARP beryllium results for MiniBooNE

The MiniBooNE (E898) experiment at Fermilab [3] was designed to address the yet unconfirmed oscillation signal reported by the LSND collaboration [4]. MiniBooNE will search for the appearance of electron neutrinos in a beam that is predominantly muon flavor with an L/E similar to LSND but with substantially differing systematics. One important systematic arises from the prediction of the fluxes of different neutrino flavors at the MiniBooNE detector.

The MiniBooNE neutrino beam is produced from the decay of π and K mesons which are produced in collisions of 8.9 GeV/c protons from the Fermilab Booster on a 71 cm beryllium target. The neutrino flux prediction is generated using a Monte Carlo simulation implemented in Geant4 [13]. Primary meson production rates are presently determined by fitting the empirical parametrization of Sanford and Wang [14] to production data in the relevant region. The results presented here, being for protons at exactly the booster beam energy, are a critical addition to the global Sanford-Wang parametrization fits.

A final flux prediction based on these data is currently being developed by the MiniBooNE collaboration and will be published by that group in the future. Here we simply demonstrate the relevance of this result in terms of coverage of the necessary kinematic phase space and neutrino flux spectrum.

Using the Monte Carlo we can illustrate the direct impact of these data on the MiniBooNE flux predictions. The dominant channel leading to a muon neutrino in the detector is $\mathrm{p+Be} \to \pi^+ \to \nu_\mu$. Fig. 19 shows the total ν_μ flux (solid) according to the simulation as well as the part coming directly from the sequence listed above (dashed). The curves are obtained from a Geant4 simulation of the booster neutrino line at Fermilab based on the parametrization of the HARP π^+ production cross-section given in Eqs. 11 and 12 and Table 3. Figure 20 shows the kinematic distribution of π^+'s which result in a ν_μ in the MiniBooNE detector. The box outlines the kinematic range of the measurements described in this paper. The simulation indicates that >80% of the relevant pions come from within this region. The neutrinos produced by the subset of pion phase-space directly covered by this measurement are shown by the dotted histogram in Fig. 19. While the coverage of these data is being displayed for the MiniBooNE detector, a similar coverage is expected for the SciBooNE detector [7] located in the same neutrino beam at Fermilab.

8   Summary and conclusions

In this paper we have presented a measurement of the double-differential production cross-section of positive pions in the collision of 8.9 GeV/c protons with a beryllium target. The data have been reported in bins of pion momentum and angle in the kinematic range from 0.75 GeV/$c \leq p_\pi \leq$ 6.5 GeV/c and 0.030 rad $\leq \theta_\pi \leq$ 0.210 rad. A systematic error analysis has been performed yielding an average point-to-point error of 9.8% (statistical + systematic) and an overall normalization error of 2%. Further, the data have been fitted to the empirical parameterization of Sanford and Wang and the resulting parameters provided.

These production data have direct relevance for the prediction of a ν_μ flux for MiniBooNE, an experiment searching for $\nu_\mu \to \nu_e$ oscillations using the Booster neutrino beam line at Fermi National Accelerator Laboratory, and SciBooNE, an experiment designed to measure ν_μ cross-sections in the 1 GeV neutrino energy region using the same beam. Final flux predictions for these experiments will be based on the results presented here and published elsewhere.
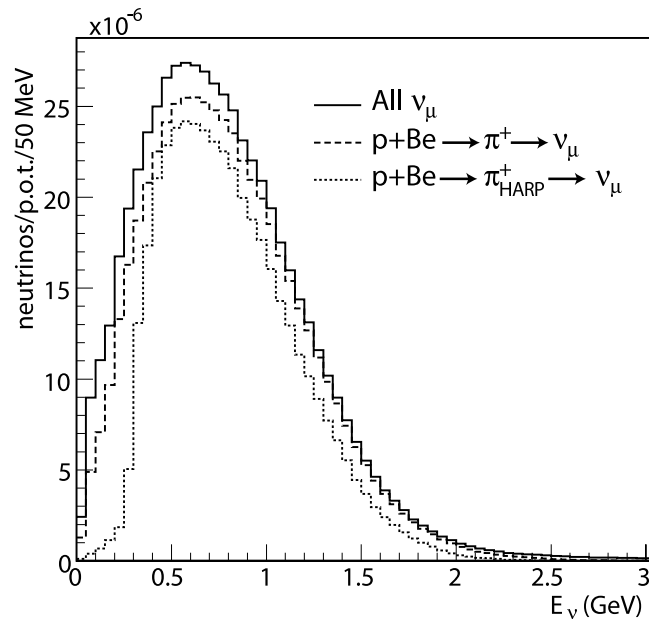
Figure 19: Predicted muon neutrino flux at the MiniBooNE detector from a Geant4 simulation of the booster neutrino line at Fermilab based on the parametrization of the HARP π^+ production cross-section (Eqs. 11 and 12 and Table 3). The solid curve is the total muon neutrino flux, while the dashed curve is the part of the ν_μ flux coming from the decay of π^+ created in proton-beryllium collisions. The primary production of positive pions is based on a parametrization of the HARP π^+ cross-section measurements presented in this paper and represents the predominant source of ν_μ at MiniBooNE. The dotted histogram shows the part of the ν_μ flux coming from the decay of π^+'s that are within the kinematic boundaries of the measurement presented here, $0.75 \text{ GeV}/c \leq p_\pi \leq 6.5 \text{ GeV}/c$ and $0.030 \text{ rad} \leq \theta_\pi \leq 0.210 \text{ rad}$.
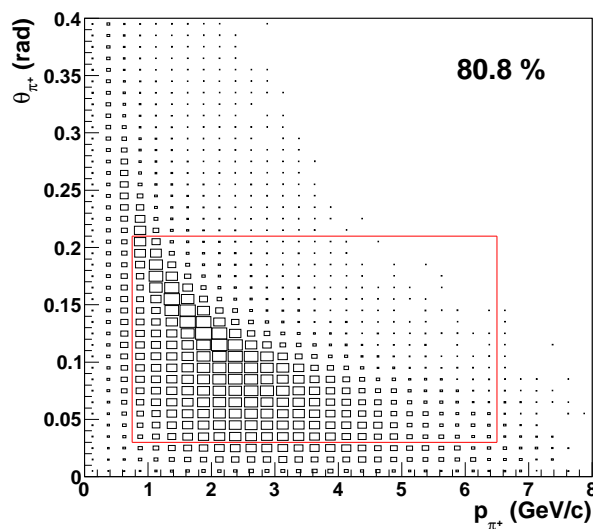

Figure 20: p-θ distribution of π^+'s which decay to a muon neutrino passing through the MiniBooNE detector according to a Monte Carlo simulation. The box marks the kinematic region of the measurement presented here and contains 80.8% of the pions contributing to the neutrino flux at MiniBooNE.

9 Acknowledgments

A   Cross-section data

$\theta_{\min}$ (mrad)	$\theta_{\max}$ (mrad)	$p_{\min}$ (GeV/c)	$p_{\max}$ (GeV/c)	$d^2\sigma^{\pi^+}/(dpd\Omega)$ (mb/(GeV/c sr))		
30	60	0.75	1.00	174.7	$\pm$	23.6
		1.00	1.25	174.8	$\pm$	24.4
		1.25	1.50	187.2	$\pm$	21.7
		1.50	1.75	180.2	$\pm$	22.5
		1.75	2.00	200.3	$\pm$	18.9
		2.00	2.25	210.5	$\pm$	17.8
		2.25	2.50	190.4	$\pm$	15.5
		2.50	2.75	180.2	$\pm$	14.7
		2.75	3.00	168.4	$\pm$	14.4
		3.00	3.25	125.3	$\pm$	10.5
		3.25	4.00	99.1	$\pm$	8.3
		4.00	5.00	64.4	$\pm$	6.9
		5.00	6.50	29.2	$\pm$	5.9
60	90	0.75	1.00	150.1	$\pm$	17.2
		1.00	1.25	161.1	$\pm$	15.5
		1.25	1.50	167.8	$\pm$	16.7
		1.50	1.75	174.6	$\pm$	17.0
		1.75	2.00	184.1	$\pm$	15.0
		2.00	2.25	186.2	$\pm$	12.1
		2.25	2.50	177.4	$\pm$	11.1
		2.50	2.75	149.7	$\pm$	9.5
		2.75	3.00	123.6	$\pm$	8.3
		3.00	3.25	92.0	$\pm$	8.0
		3.25	4.00	68.8	$\pm$	5.4
		4.00	5.00	43.2	$\pm$	3.9
		5.00	6.50	17.5	$\pm$	2.8
90	120	0.75	1.00	180.7	$\pm$	17.3
		1.00	1.25	178.8	$\pm$	18.4
		1.25	1.50	180.2	$\pm$	13.1
		1.50	1.75	146.1	$\pm$	13.0
		1.75	2.00	142.2	$\pm$	12.8
		2.00	2.25	126.9	$\pm$	10.3
		2.25	2.50	118.8	$\pm$	8.5
		2.50	2.75	95.2	$\pm$	7.0
		2.75	3.00	73.8	$\pm$	6.8
		3.00	3.25	57.9	$\pm$	5.5
		3.25	4.00	43.7	$\pm$	3.3
		4.00	5.00	22.9	$\pm$	2.8
		5.00	6.50	8.3	$\pm$	1.5

Table 5: HARP results for the double-differential π^+ production cross-section in the laboratory system, $d^2\sigma^{\pi^+}/(dpd\Omega)$. Each row refers to a different $(p_{\min} \leq p < p_{\max}, \theta_{\min} \leq \theta < \theta_{\max})$ bin, where p and θ are the pion momentum and polar angle, respectively. The central value as well as the square-root of the diagonal elements of the covariance matrix are given.

$\theta_{\min}$ (mrad)	$\theta_{\max}$ (mrad)	$p_{\min}$ (GeV/c)	$p_{\max}$ (GeV/c)	$d^2\sigma^{\pi^+}/(dpd\Omega)$ (mb/(GeV/c sr))		
120	150	0.75	1.00	168.7	$\pm$	16.9
		1.00	1.25	155.3	$\pm$	16.5
		1.25	1.50	153.7	$\pm$	13.2
		1.50	1.75	142.9	$\pm$	11.1
		1.75	2.00	118.4	$\pm$	9.6
		2.00	2.25	97.1	$\pm$	8.4
		2.25	2.50	86.0	$\pm$	6.6
		2.50	2.75	66.4	$\pm$	6.5
		2.75	3.00	54.6	$\pm$	5.5
		3.00	3.25	45.2	$\pm$	4.8
		3.25	4.00	27.6	$\pm$	3.2
		4.00	5.00	13.5	$\pm$	2.2
		5.00	6.50	4.9	$\pm$	0.8
150	180	0.75	1.00	165.2	$\pm$	20.3
		1.00	1.25	173.9	$\pm$	15.7
		1.25	1.50	143.8	$\pm$	15.4
		1.50	1.75	116.1	$\pm$	10.8
		1.75	2.00	97.4	$\pm$	8.6
		2.00	2.25	68.2	$\pm$	6.1
		2.25	2.50	52.1	$\pm$	5.6
		2.50	2.75	41.5	$\pm$	3.8
		2.75	3.00	35.0	$\pm$	3.8
		3.00	3.25	24.8	$\pm$	3.0
		3.25	4.00	17.4	$\pm$	2.1
		4.00	5.00	7.8	$\pm$	1.2
		5.00	6.50	2.8	$\pm$	0.3
180	210	0.75	1.00	171.3	$\pm$	29.8
		1.00	1.25	131.9	$\pm$	15.0
		1.25	1.50	101.6	$\pm$	12.3
		1.50	1.75	63.5	$\pm$	8.9
		1.75	2.00	49.2	$\pm$	6.7
		2.00	2.25	39.7	$\pm$	5.1
		2.25	2.50	28.1	$\pm$	4.2
		2.50	2.75	21.8	$\pm$	3.0
		2.75	3.00	15.6	$\pm$	2.2
		3.00	3.25	13.1	$\pm$	1.8
		3.25	4.00	9.9	$\pm$	1.3
		4.00	5.00	5.6	$\pm$	0.8
		5.00	6.50	1.8	$\pm$	0.4

References

[1] M. H. Ahn *et al.* [K2K Collaboration], "Measurement of neutrino oscillation by the K2K experiment", Phys. Rev. D **74** (2006) 072003 [arXiv:hep-ex/0606032].

[2] Y. Ashie *et al.* [Super-Kamiokande Collaboration], "A measurement of atmospheric neutrino oscillation parameters by Super-Kamiokande I", Phys. Rev. D **71** (2005) 112005 [arXiv:hep-ex/0501064].

[3] E. Church *et al.* [BooNe Collaboration], "A proposal for an experiment to measure muon-neutrino → electron-neutrino oscillations and muon-neutrino disappearance at the Fermilab Booster: BooNE", FERMILAB-PROPOSAL-0898.

[4] A. Aguilar *et al.* [LSND Collaboration], "Evidence for neutrino oscillations from the observation of anti-nu/e appearance in a anti-nu/mu beam", Phys. Rev. D **64** (2001) 112007 [arXiv:hep-ex/0104049].

[5] M. G. Catanesi *et al.* [HARP Collaboration], "The HARP Detector at the CERN PS", Nucl. Instrum. Meth. A **571** (2007) 527.

[6] M. Anfreville *et al.*, "The drift chambers of the NOMAD experiment", Nucl. Instrum. Meth. A **481** (2002) 339. [arXiv:hep-ex/0104012].

[7] A. A. Aguilar-Arevalo *et al.* [SciBooNE Collaboration], "Bringing the SciBar detector to the Booster neutrino beam", [arXiv:hep-ex/0601022].

[8] M. G. Catanesi *et al.* [HARP Collaboration], "Measurement of the production cross-section of positive pions in p Al collisions at 12.9-GeV/c", Nucl. Phys. B **732** (2006) 1 [arXiv:hep-ex/0510039].

[9] M. G. Catanesi *et al.* [HARP Collaboration], "Particle identification algorithms for the HARP forward spectrometer", accepted by Nucl. Instrum. Meth. A.

[10] M. Baldo-Ceolin *et al.*, "The Time-Of-Flight TOFW Detector Of The HARP Experiment: Construction And Performance", Nucl. Instrum. Meth. A **532** (2004) 548.

[11] G. Folger, V. N. Ivanchenko, J. P. Wellisch, "The Binary cascade", Eur. Phys. Jour. A21 (3) (2004) 407.

[12] A. Heikkinen, N. Stepanov and J. P. Wellisch, "Bertini intra-nuclear cascade implementation in Geant4," In the Proceedings of 2003 Conference for Computing in High-Energy and Nuclear Physics (CHEP 03), La Jolla, California, 24-28 Mar (2003), pp MOMT008 [arXiv:nucl-th/0306008].

[13] S. Agostinelli *et al.* [GEANT4 Collaboration], "GEANT4: A simulation toolkit", Nucl. Instrum. Meth. A **506** (2003) 250.

[14] J. R. Sanford and C. L. Wang, "Empirical formulas for particle production in p-Be collisions between 10 and 35 BeV/c", Brookhaven National Laboratory, AGS internal report, (1967) (*unpublished*).